Effects of spalled particles thermal degradation on a hypersonic flow field environment

Raghava S. C. Davuluri[a], Huaibao Zhang[b], Kaveh A. Tagavi[a], Alexandre Martin[a,*]

[a]*Mechanical and Aerospace Engineering, University of Kentucky, Lexington, KY, 40506, USA*
[b]*School of Aeronautics and Astronautics, Sun Yat-Sen University, Guangzhou 510006, China*

Abstract

The presence of spalled particles might affect the flow field and the material, thereby influencing the aerodynamic heating rates of the thermal protection system. In order to study the impact of particles on the flowfield, a two-way coupling is performed between a Lagrangian particle trajectory model and a hypersonic aerothermodynamics flow solver. Time-accurate solutions are computed for argon and air flowfields. Single-particle and multiple-particle simulations are performed and results are studied. The studies in the argon environment indicated that the particles start sublimating soon after they cross the shock and keep sublimating during the remainder of their time in the flow. In the air environment, the particles start releasing carbon vapor soon after their ejection, and the magnitudes of different carbon products vary based on the particle's location relative to the shock. Similar behavior is observed for multiple-particle simulations but with an increase in the amount of released carbon vapor that diffuses and convects over a larger area. A single-particle simulation is also run by adding additional gas phase reactions, and it is found that the production rate of certain carbon products (C_1 and CN) increases. A parametric study is conducted based on parameters that affect the motion of the particles. The results of the comprehensive study show that the carbon vapor released by spalled particles tends to change the composition of the flow field, particularly the upstream region of the shock, which affects the heat flux incident on the test sample.

Keywords: Spallation, Ablation, Thermal Protection System, Time Accurate Solutions, Lagrangian Particle Trajectory, Particle-laden flows, Aerothermodynamics

Nomenclature

Symbols

A	Face area, m^2
E	Specific total energy, J/kg

*Corresponding author
Email addresses: raghava.davuluri@uky.edu (Raghava S. C. Davuluri), zhanghb28@mail.sysu.edu.cn (Huaibao Zhang), kaveh.tagavi@uky.edu (Kaveh A. Tagavi), alexandre.martin@uky.edu (Alexandre Martin)

E_{ve}	Specific vibrational-electron-electronic energy, J/kg
F_D	Drag force, N
$\boldsymbol{\mathcal{F}_c}$	Convective flux matrix
$\boldsymbol{\mathcal{F}_d}$	Diffusive flux matrix
h	Enthalpy, J/mol
$\mathbf{J_i}$	Mass diffusive flux, kg/(m^2–s)
M	Mach number
$\dot{m}_{C/i}$	Mass production rate due to surface reactions, kg/s
m_p	Mass of the particle, kg
M_w	Molar mass, kg/mol
$\mathbf{n}$	Normal face vector
$\mathbf{P}$	Primitive variables vector
p	Static pressure, N/m^2
p_{drag}	Drag power, J/s
$\mathbf{Q}$	Conservative variables vector
$\mathbf{q}$	Heat flux vector
$\dot{q}$	Heat transfer rate, J/s
$\mathbf{R}$	Residual vector
$\mathbf{S}$	Source term vector in KATS
t	Time, s
T	Temperature, K
(u, v, w)	Velocity components in axial, radial and z-directions, m/s
$\mathbf{U}$	State vector
V	Volume of the mesh cell, m^3
$\mathbf{W}$	Source vector
(x, y, z)	Position components in axial, radial and z-directions, m
ρ	Density, kg/m^3
$\boldsymbol{\tau}$	Viscous tensor
$\dot{\omega}$	Mass production rate in KATS, kg/s

Subscripts

conv	Convection
f	Flow field
g	gas phase

p	Particle
rad	Radiation
rxn	Chemical reaction
s	solid phase
tr	translational-rotational energy mode
ve	vibrational-electronic energy mode

1. Introduction

Ablative thermal protection system materials shield entry vehicles from high heat loads through the combination of heat and mass transfer phenomena usually referred to as "ablation." As the surface of the material undergoes chemical transformation, mostly through oxidation, it has been observed that solid particles are ejected from the surface into the flow. This process – typically included in the ablation umbrella term – is defined as "spallation." It is believed that the thermal, mechanical shear and inner pressure stresses cause the ejection of the particles. The spalled particles are likely produced by disconnected fibers or chunks of material, although they could also be formed from soot, a by-product of the pyrolysis of the resin that constitutes heat shield material.

The presence of spalled particles around the material is believed to affect the flow field, and thus the surface heating rates since the near-surface chemistry is modified. Moreover, the particles' ejections take place before the material fully oxidizes, thereby increasing the heat rates at the surface and accelerating the material recession. The particles travel through a high-temperature zone and re-radiate energy back to the surface as they heat up, thus increasing the heat flux onto the capsule. Through these phenomena, spallation affects the ablative material directly. Additionally, the particles also tend to react chemically and physically with the species in the flow along their paths, thus changing the chemical composition of the flow field, and hence altering the radiative heat flux.

Discrepancies were found when experimentally measured heating rates and temperature profiles of Pioneer-Venus [1] and Galileo Probe [2, 3, 4] heat shields were compared with the theoretical predictions. The value of the parameters was over-predicted near the stagnation point and under-predicted in the downstream region. Although the experimental results were re-evaluated by varying the effect of turbulence, no reasonable explanation was found for the discrepancy. The results suggested that additional mechanisms caused an increase in radiation or turbulence in the downstream region. Spallation was believed to be one of those mechanisms. Furthermore, when laser attenuation and emission spectroscopy measurements were performed by Raiche and Driver [5], the results were unexpected as it was found that with an increase in heating rates, the optical attenuation increased for a PICA sample. This unexpected phenomenon was speculated to be due to the

scattering, absorptive and reflective nature of spalled particles. Also, the optical emissions in the inviscid region corresponded to black body radiation at about 3800 K and were likely due to the presence of spalled particles. Spectroscopic measurements by Yoshinaka [6] on ablating models in air flow field demonstrated the presence of CN emission spectra in the upstream region of the surface. Similar spectroscopic experiments by Kihara et al. [7] in the region ahead of the shock detected the presence of CN emission spectra in the nitrogen and air environments and the presence of C emission spectra in the argon environment. The most likely reason for the presence of CN and C in the upstream region of the shock is due to spalled particles, as they are the only carbon source that can reach a distance that far from the sample.

Based on above experimental observations, numerical models [8, 9, 7, 10] were developed to compute the dynamics of spalled particles. These models used the extracted flow field data to study the spallation behavior. Pace et al. [11] developed an Eulerian particle model of uniform mass, and loosely coupled it to Computational Fluid Dynamics (CFD) code DPLR (Data Parallel Line Relaxation) [12], to evaluate the impact of spalled particles on radiative heating.

Following these studies, a Lagrangian particle trajectory model [13] was recently developed to compute the properties of the spalled particles. The code takes into account the chemical reactivity of the particles with the flow field species. The code was one-way coupled in previous work to the Fluid Dynamics (FD) module of Kentucky Aerothermodynamic and Thermal-response Solver (KATS) [14] to evaluate the effect of flow field on the spalled particles. In order to assess the effect of spalled particles on the flow field, a two-way coupling between the spallation model and KATS-FD model is performed and is presented here. The coupling is performed for a single particle and for multiple particles in argon and air environments. Additionally, a parametric study is conducted for single particle simulation in air environment to summarize the effect based on the parameters that govern the particle's motion. It should be noted that the trajectories presented in the present work might not represent the ones from spallation experiments [15, 16, 17]. However, the main objective of the present work is to assess the impact of particle dynamics on flow field and not necessarily to replicate the experimental trajectories. It is for the same reason only gas-particle interactions and no other ablative mechanisms are considered in this work.

2. Methodology

2.1. Numerical models

2.1.1. KATS – FD

The thermo-chemical non-equilibrium flow field in the continuum regime is computed using KATS-FD [18], a laminar hypersonic aerothermodynamic modified Navier-Stokes CFD solver. The governing equation of the model is of the form:

$$\frac{\partial \mathbf{Q}}{\partial t} + \nabla \cdot (\boldsymbol{\mathcal{F}} - \boldsymbol{\mathcal{F}_d}) = \mathbf{S}_f \tag{1}$$

where $\mathbf{Q}$ is a vector of conservative variables, $\boldsymbol{\mathcal{F}}$ and $\boldsymbol{\mathcal{F}_d}$ are convective and diffusive flux matrices, respectively, and $\mathbf{S}_f$ is the source term vector. The weak form of the governing equation (Eq. (1)) is obtained by integrating it over a finite volume V for an arbitrary mesh cell and is given by:

$$\int_V \frac{\partial \mathbf{Q}}{\partial t}\, dV + \oint_A (\boldsymbol{\mathcal{F}} - \boldsymbol{\mathcal{F}_d}) \cdot \mathbf{n}\, dA = \int_V \mathbf{S}_f\, dV \tag{2}$$

where the Gauss theorem has been applied to the flux term. Assuming uniform physical properties within the control volume, the left-hand side term of the equation is integrated with respect to time by employing the first-order backward Euler method, and integration of the flux integral is performed by adding the fluxes across each surface. The final form of the equation is

$$\left[\frac{V}{\Delta t}\left(\frac{\partial \mathbf{Q}}{\partial \mathbf{P}}\right)^n - \left(\frac{\partial \mathbf{R}}{\partial \mathbf{P}}\right)^n\right] \Delta \mathbf{P} = \mathbf{R}^n \quad . \tag{3}$$

where $\mathbf{P}$ is a vector of primitive variables, Δt is the time step size, and $\mathbf{R}$ is the residual vector which is expressed as:

$$\mathbf{R} \equiv \sum_{j \in cell} (\boldsymbol{\mathcal{F}_d} - \boldsymbol{\mathcal{F}}) \cdot \mathbf{n}_j\, A_j + V\, \mathbf{S}_f \tag{4}$$

where $\mathbf{n}$ and A are the face normal and face area respectively. The vectors of conservative variables, primitive variables, and source terms are of the forms:

$$\mathbf{Q} = \begin{pmatrix} \rho_1 \\ \vdots \\ \rho_{ngs} \\ \rho_g u \\ \rho_g v \\ \rho_g w \\ \rho E \\ \rho E_{ve} \end{pmatrix}, \qquad \mathbf{P} = \begin{pmatrix} \rho_1 \\ \vdots \\ \rho_{ngs} \\ u \\ v \\ w \\ T \\ T_{ve} \end{pmatrix}, \qquad \mathbf{S}_f = \begin{pmatrix} \dot{\omega}_1^f \\ \vdots \\ \dot{\omega}_{ngs}^f \\ 0 \\ 0 \\ 0 \\ 0 \\ \dot{\omega}_{ve}^f \end{pmatrix} \tag{5}$$

where ρ_i is the density of species i, (u, v, w) are the components of bulk velocity, and E and E_{ve} are the total energy and vibrational-electron-electronic energy per unit mass characterized by temperatures T and T_{ve}, respectively. $\dot{\omega}_i^f$ is the mass production rate of species i and $\dot{\omega}_{ve}^f$ is the vibrational energy transfer rate between two different energy modes. Subscripts 1 to ngs represent the species number, while subscript g

represents the gas mixture. The convective and diffusive flux matrices in Eq. (1) are given as:

$$\boldsymbol{\mathcal{F}} = \begin{pmatrix} \rho_1 u & \rho_1 v & \rho_1 w \\ \vdots & \vdots & \vdots \\ \rho_{ngs} u & \rho_{ngs} v & \rho_{ngs} w \\ \rho_g u^2 + p & \rho_g vu & \rho_g wu \\ \rho_g uv & \rho_g v^2 + p & \rho_g wv \\ \rho_g uw & \rho_g vw & \rho_g w^2 + p \\ (\rho E + p)\, u & (\rho E + p)\, v & (\rho E + p)\, w \end{pmatrix}, \; \boldsymbol{\mathcal{F}_d} = \begin{pmatrix} & -\mathbf{J}_1 & \\ & \vdots & \\ & -\mathbf{J}_{ngs} & \\ \tau_{xx} & \tau_{xy} & \tau_{xz} \\ \tau_{yx} & \tau_{yy} & \tau_{yz} \\ \tau_{zx} & \tau_{zy} & \tau_{zz} \\ & \tau\mathbf{u} - \mathbf{q} - \sum_{\mathbf{i=1}}^{\mathbf{ngs}} (\mathbf{J_i h_i}) & \end{pmatrix} \tag{6}$$

where p is the static pressure, $\boldsymbol{\tau}$ is the viscous tensor, $\mathbf{J_i}$ is the diffusive flux of species i, and $\mathbf{q}$ is the heat flux vector. The code employs second-order spatial discretization and first-order temporal integration.

2.1.2. Lagrangian particle trajectory model

The model simulates the dynamics of a spalled particle by employing a Lagrangian formulation [19]. The model also includes the chemical interaction of the particle with the flow field. The governing equation of the model is

$$\frac{\partial \mathbf{U}}{\partial t} = \mathbf{W} \tag{7}$$

where $\mathbf{U}$ is the state vector and $\mathbf{W}$ is the source term vector. The elements of the vectors are represented as:

$$\mathbf{U} = \begin{pmatrix} m_p \\ m_p u_p \\ m_p v_p \\ m_p w_p \\ m_p E_p \end{pmatrix}, \qquad \mathbf{W} = \begin{pmatrix} \dot{m}_{\mathrm{C}} \\ F_{D_x} \\ F_{D_y} \\ F_{D_z} \\ \dot{q}_{conv} + p_{drag} - \dot{q}_{rad} + \dot{q}_{rxn} \end{pmatrix} \tag{8}$$

where m_p is the mass of the particle, (u_p, v_p, w_p) are velocity components of the particle, E_p is the specific total energy of the particle, $\dot{m}_{\mathrm{C}}$ is the mass source term, $\left(F_{D_x}, F_{D_y}, F_{D_z}\right)$ are components of drag force acting on the particle, and $\dot{q}_{conv}$, $\dot{q}_{rad}$, $\dot{q}_{rxn}$, p_{drag} are convective, radiative, reaction heat rates, and power drag. The reactions at the particle surface considered in this model are oxidation, nitridation, and sublimation. The reactions are irreversible in nature and are given in Table 1.

The mass recession rates due to oxidation and nitridation are computed by employing parameters from Driver's chemistry model [20, 21], whereas the Knudsen-Langmuir equation [22] is used to calculate the surface recession rate due to sublimation. Therefore, the final form of the mass source term can be expressed as:

$$\dot{m}_{\mathrm{C}} = -\dot{m}_{\mathrm{C/CO}} - \dot{m}_{\mathrm{C/CN}} - \dot{m}_{\mathrm{C/C_1,C_2,C_3}} \tag{9}$$

Table 1: Surface chemistry model considered for Spallation model

Type	Reaction
Oxidation	$\mathrm{C(s) + O \longrightarrow CO}$
Oxidation	$\mathrm{2\,C(s) + O_2 \longrightarrow 2\,CO}$
Nitridation	$\mathrm{C(s) + N \longrightarrow CN}$
Sublimation	$\mathrm{C(s) \longrightarrow C_1}$
Sublimation	$\mathrm{2\,C(s) \longrightarrow C_2}$
Sublimation	$\mathrm{3\,C(s) \longrightarrow C_3}$

where $\dot{m}_{C/i}$ denotes the mass recession rates due to the reaction producing species i.

2.2. Two-way coupling method

The two-way coupling scheme is performed by adding a source term vector $\mathbf{S}_p$ to Eq. (1), which accounts for the particle's contributions that affect the fluid. Therefore, the modified form of the governing equation of KATS-FD can be expressed as

$$\frac{\partial \mathbf{Q}}{\partial t} + \nabla \cdot (\boldsymbol{\mathcal{F}} - \boldsymbol{\mathcal{F}}_{\boldsymbol{d}}) = \mathbf{S}_f + \mathbf{S}_p \tag{10}$$

The elements of $\mathbf{S}_p$ are represented as

$$\mathbf{S}_p = \begin{pmatrix} \dot{\omega}_1^p \\ \vdots \\ \dot{\omega}_{ngs}^p \\ \dot{\omega}_{mom,x}^p \\ \dot{\omega}_{mom,y}^p \\ \dot{\omega}_{mom,z}^p \\ \dot{\omega}_{tr}^p \\ 0 \end{pmatrix} \tag{11}$$

where $\dot{\omega}_i^p$ is the mass rate of species produced or consumed due to surface reactions, $\dot{\omega}_{mom,i}^p$ is the rate of change of momentum, and $\dot{\omega}_{tr}^p$ is the rate of change of total energy of the particle.

2.2.1. Solution technique

Initially, a steady state solution is computed for the flow field environment using KATS-FD. The flow field parameters are then used by the spallation model to calculate the dynamics of the particle. The two-way coupling is achieved by inserting the elements of source term vector $\mathbf{W}$ into the source term vector $\mathbf{S}_p$ of the CFD code. The coupling is performed according to the following:

- **Mass coupling**

  The products released from the surface reactions of the particle tend to affect the composition of the flow field environment. The mass recession rate due to the spalled particle is inserted into the CFD code as:

$$\dot{\omega}_i^p = \frac{\dot{m}_{\mathrm{C}/i}}{V} \qquad (i = \mathrm{CO}, \mathrm{CN}, \mathrm{C}_1, \mathrm{C}_2, \mathrm{C}_3) \tag{12}$$

  where V is the volume of the mesh cell in which the spalled particle is present [23, 24]. The mass coupling also accounts for the change in concentrations of oxygen (atomic and molecular) and atomic nitrogen responsible for the particle surface reactions, which are given as:

$$\dot{\omega}_{\mathrm{O}}^p = -\left(\frac{M_{w\mathrm{O}}}{M_{w\mathrm{C}}}\right)\frac{\dot{m}_{\mathrm{C/CO}}}{V} \tag{13}$$

$$\dot{\omega}_{\mathrm{N}}^p = -\left(\frac{M_{w\mathrm{N}}}{M_{w\mathrm{C}}}\right)\frac{\dot{m}_{\mathrm{C/CN}}}{V} \tag{14}$$

$$\dot{\omega}_{\mathrm{O}_2}^p = -0.5\left(\frac{M_{w\mathrm{O}_2}}{M_{w\mathrm{C}}}\right)\frac{\dot{m}_{\mathrm{C/CO}}}{V} \tag{15}$$

  where M_{wi} is the molar mass of species i.

- **Momentum coupling**

  The motion of the spalled particle is affected by the drag force acting on it. Hence, momentum coupling deals with reaction of drag force on the flow field. The elements of $\mathbf{S}_p$ corresponding to the momentum terms determined from the spallation model are:

$$\dot{\omega}_{mom,i}^p = -\frac{F_{D_i}}{V} \tag{16}$$

  where i refers to the x-, y-, and z-directions.

- **Energy coupling**

  The energy rate terms of the spalled particle from the vector $\mathbf{W}$ which affect the flow field are $\dot{q}_{conv}$, p_{drag}, and $\dot{q}_{rxn}$. The convective heat rate ($\dot{q}_{conv}$) accounts for the heat transfer rate between the flow gases and the spalled particle. The heat energy released or absorbed due to particle reactions per unit time ($\dot{q}_{rxn}$) affects the temperature of the flow field. Also, the work done by the particle to overcome the drag force (p_{drag}) affects the kinetic energy of the flow field. Hence, the energy coupling is performed by inserting the energy rate terms from $\mathbf{W}$ into $\mathbf{S}_p$ as:

$$\dot{\omega}_{tr}^p = -\frac{\dot{q}_{conv} + p_{drag} + \dot{q}_{rxn}}{V} \tag{17}$$

  It is assumed that the radiative heat rate from the particle impacts the ablative material, and is less effective on the flow field. Hence, $\dot{q}_{rad}$ term is not considered in the energy coupling.

Starting from the initially converged CFD solution, KATS is used in a transient mode, and the spallation source terms are added to the cell centers as given by Eqs. (12) – (17) along the path of the particle. To maintain a time-accurate solution, the Courant-Friedrichs-Lewy (CFL) number in the CFD code is kept under 1.

2.2.2. Cell location algorithm

The source vector $\mathbf{S}_p$ is computed at the cell centers of the mesh, whereas the spallation model provides results based on nodal properties. A new algorithm was developed to locate the center of the mesh cell in which the spalled particle is present. Using the algorithm, the source terms calculated by the spallation code are added to the center of the cell in which the particle is present. Figure 1 illustrates the trajectory of a 30 µm particle ejected normally from the surface, 5 mm from the center axis, at an initial velocity of 90 m/s in the air flowfield. The cell centers located by the new algorithm, denoted by red squares, are shown at three different locations with respect to the position of the particle.

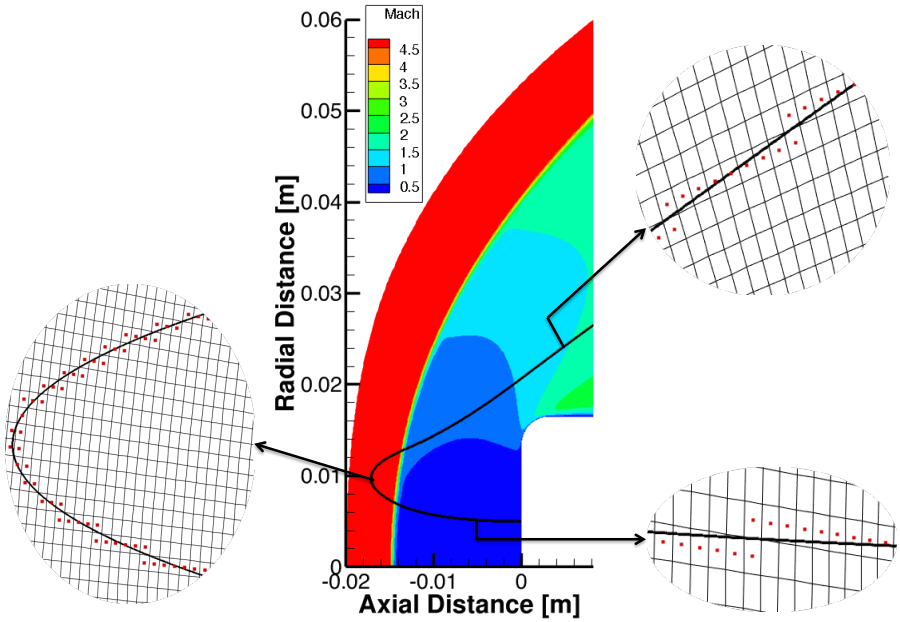

Figure 1: Cell-centers located with respect to the trajectory of the particle

2.2.3. Verification

To verify that an accurate coupling procedure was employed, a constant spallation source term was added to a zero velocity flow field. An integration was performed over the cell volumes to evaluate the mass

deposited by the spalled particle in the flow field. It was verified that the mass deposited in the flow field was equal to the total mass added from the source term file (constant source term $\times$ time step size $\times$ total time steps). Since the mass added by the spallation code was equivalent to the mass deposited in the flow field, the applied coupling method was considered verified. Figure 2 shows a time-accurate solution of zero velocity flow field when a 14 μm particle is ejected with a velocity of 370 m/s normally, 13 mm from the center axis. The particle deposits a source term of magnitude 10^{-18} kg/s throughout its travel. The particle trajectory takes 2697 iterations of time step size 1×10^{-7} s to complete. Figure 2 corresponds to the solution after 600 time steps. The values of numerically calculated mass (mass integrated over cell volumes), theoretical mass, and their relative error for various iterations are given in Table 2.

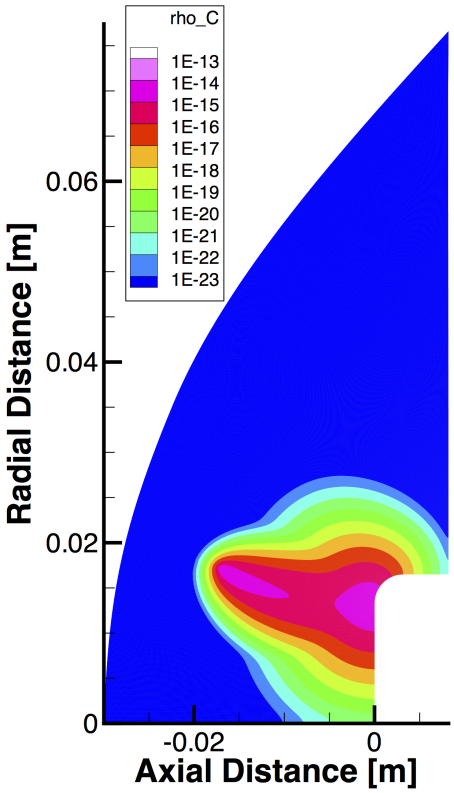

Figure 2: Carbon vapor deposited in a zero-velocity flow field after 600 time-steps

The mass deposited by the particle is transported through the flow field by advection and diffusion. The chemical vapor produced is advected in the direction of the bulk velocity of the fluid, and is diffused in the direction of the density gradient. In this particular case, since it is a zero velocity flow field, the mass deposited is not advected and is only propagated by diffusion along the particle trajectory.

Table 2: Verification results

Iterations	Numerical Mass (kg)	Theoretical Mass (kg)	Absolute error (kg)
0	1.83E-36	0.00E+00	1.83E-36
100	1.00E-23	1.00E-23	2.28E-26
200	2.00E-23	2.00E-23	8.70E-28
300	3.00E-23	3.00E-23	8.22E-27
400	4.00E-23	4.00E-23	2.14E-26
500	5.00E-23	5.00E-23	3.69E-26
600	6.00E-23	6.00E-23	3.75E-26
700	7.00E-23	7.00E-23	4.38E-26

3. Results and discussion

The time-accurate two-way coupling solutions were computed for Mach 5 high enthalpy Argon and Air environments. The boundary conditions used to compute the steady state solution for the argon environment are given in Table 3. These conditions correspond to the flow of specific total enthalpy of 8.06 MJ/kg and result in a cold-wall heat flux of 246 W/cm^2 and pressure of 23.343 kPa at the stagnation point. It should be noted that the ionization reactions of argon are not included for the simulation, resulting in a flow field solution with higher temperatures and greater shock stand-off distance.

Table 3: Uniform flow conditions of Mach 5 argon flow

ρ_f (kg/m^3)	U_∞ (m/s)	T_{tr} (K)	T_w (K)
3.45×10^{-3}	3860.0	1470	500

The flow conditions considered to compute the steady state solution for the air environment are presented in Table 4. These conditions yield a flow of specific total enthalpy 5.6 MJ/kg that would result in a cold wall heat flux and pressure of 74 W/cm^2 and 7.155 kPa, respectively, at the stagnation point.

Table 4: Uniform flow conditions and mole fractions of species of Mach 5 air flow

ρ_f (kg/m^3)	U_∞ (m/s)	T_{tr} (K)	T_{ve} (K)	T_w (K)	Y_{Ar}	$Y_{\mathrm{N_2}}$	$Y_{\mathrm{O_2}}$	Y_{NO}	Y_{O}	Y_{N}
1.49×10^{-3}	3162.7	896	896	600	0.047	0.686	0.051	0.042	0.000	0.173

Simulations for a single particle as well as for multiple particles were performed. For the case of the single particle simulation, the coupling was performed in three stages: only mass, mass and energy coupling, and

total (mass, momentum, and energy) coupling. This systematic procedure helps track changes in flow field properties. For the multiple particles simulation, only the total coupling was performed.

3.1. Single-particle simulation

3.1.1. Argon flow field

The mass decrease of the spalled particle while traveling in the argon environment only occurs through sublimation. The ejection parameters and the total physical time taken by the particle to travel through the computational domain are given in Table 5. The physical time mentioned hereafter denotes the time taken by the particle to travel from its ejection point until it exits the computational domain.

Table 5: Ejection parameters and physical time for single particle simulation in argon environment

Size (μm)	Velocity (m/s)	Position (mm)	Angle (°)	Physical time (ms)
14	370	(0,13,0)	0	0.2697

To ensure time accuracy, the solution was computed with the time step size of 4×10^{-9} s, which corresponds to a maximum CFL of 0.824. The results for mass coupling of the particle given in Table 5 are illustrated in Figs. 3, 4, 5, and 6. These figures consist of a temperature profile and density profiles (C_1, C_2, and C_3) at different travel times. The temperature profile is used to indicate the position of the particle with respect to shock location, whereas the density profiles are used to determine the mass of the vapor deposited by the spalled particle. The animation of this simulation is provided in the Supplementary Material.

Sublimation is only a function of the temperature of the particle. Due to the very low thermal conductivity of argon, the thermal interaction between the particle and flow field is negligible. At 0.07 ms into the particle's travel, its temperature remains relatively low, resulting in negligible recession. This can be observed in Fig. 3.

The temperature of the spalled particle increases while it crosses the shock. At about 0.15 ms of travel time, the particle starts sublimating, as seen in Fig. 4. Owing to a high temperature, the released vapor is diffused rapidly into the flow field. Additionally, the bulk velocity of the fluid guides the diffused vapor along the downstream region of the shock.

At 0.20 ms of travel time, the particle is in the upstream region of the shock and is about to re-enter (Fig. 5). With an increase in the particle's surface temperature, it sublimates more vapor, thus increasing the concentration of the sublimed vapor.

This diffused carbon vapor increases in magnitude when the particle is in the downstream region, immediately after re-entering the post-shock region. Figure 6 shows the particle at 0.26 ms travel time, with the additional concentration of carbon species around it.

It can be seen from the above simulation that the order of magnitude of diffused vapor decreases from C_3 species to C_1 species. It can be concluded that when the particle sublimates, the concentration of C_3

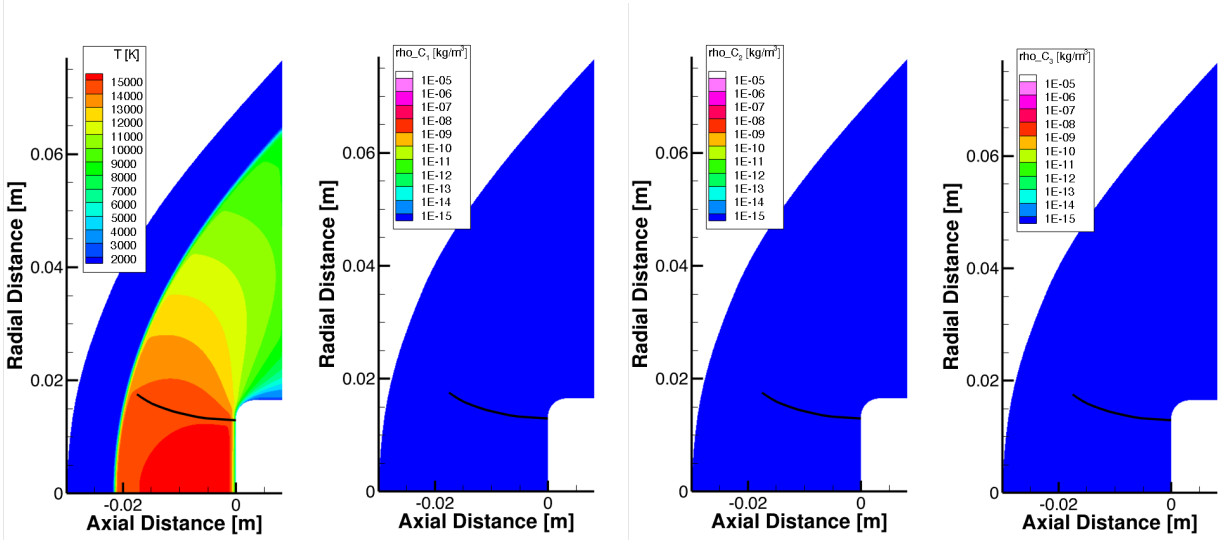

(a) Temperature (b) C_1 Density (c) C_2 Density (d) C_3 Density

Figure 3: Trajectory of the particle in an argon flow field at 0.07 ms with heterogeneous carbon reactions. (An animation of this figure is provided in the Supplementary Material.)

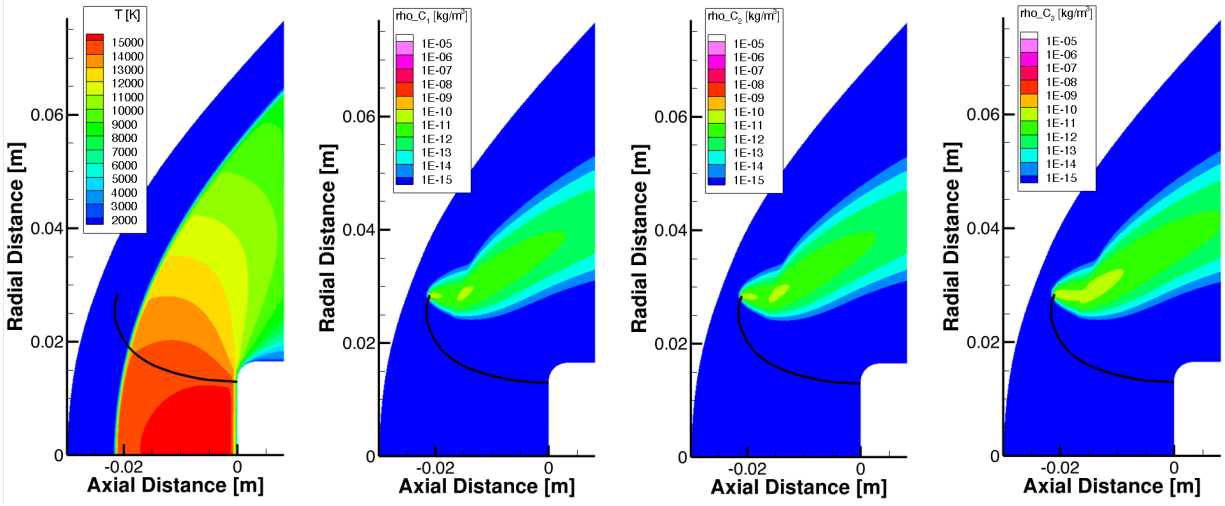

(a) Temperature (b) C_1 Density (c) C_2 Density (d) C_3 Density

Figure 4: Trajectory of the particle in an argon flow field at 0.15 ms with heterogeneous carbon reactions. (An animation of this figure is provided in the Supplementary Material.)

vapor dominates other species.

The simulation results for the mass and energy coupling and the total coupling are virtually identical to

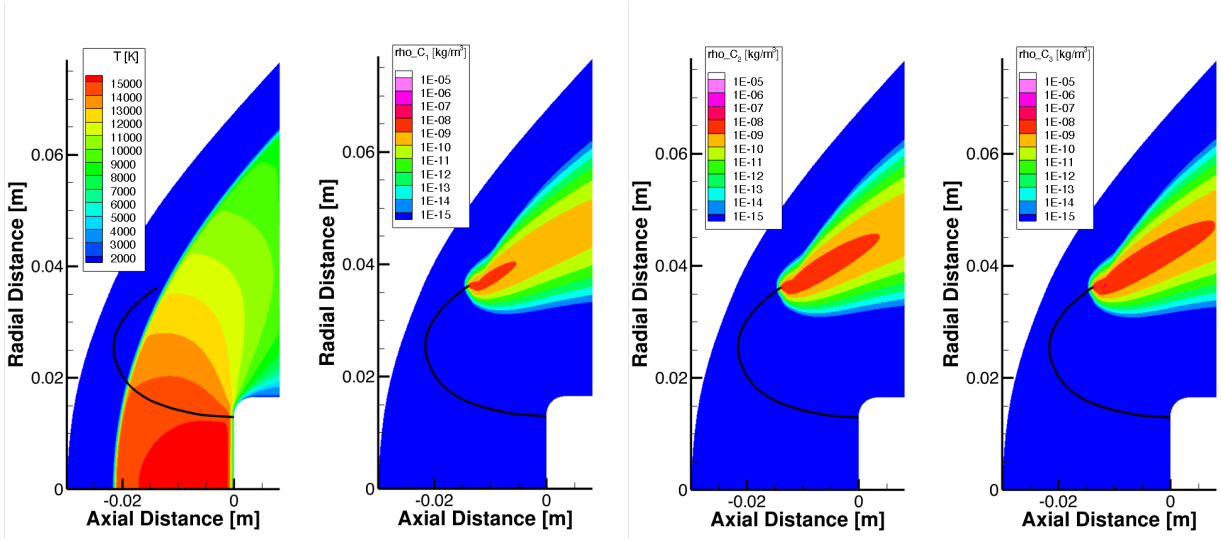

(a) Temperature (b) C_1 density (c) C_2 density (d) C_3 density

Figure 5: Trajectory of the particle in an argon flow field at 0.20 ms with heterogeneous carbon reactions. (An animation of this figure is provided in the Supplementary Material.)

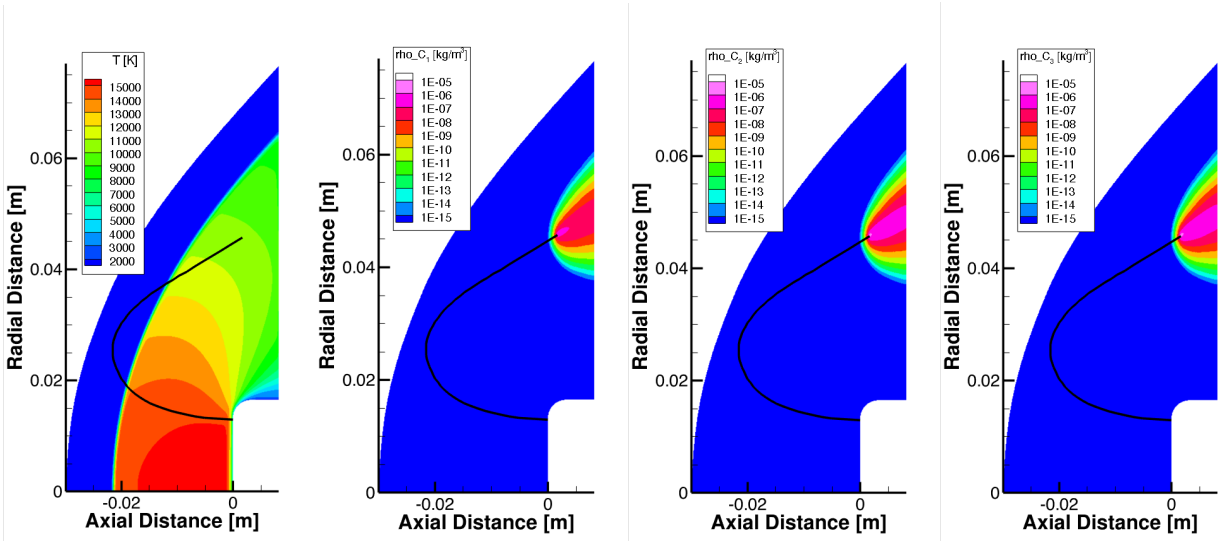

(a) Temperature (b) C_1 density (c) C_2 density (d) C_3 density

Figure 6: Trajectory of the particle in an argon flow field at 0.26 ms with heterogeneous carbon reactions. (An animation of this figure is provided in the Supplementary Material.)

the ones obtained for mass coupling. The temperature varies by 0.01 K and no change is detected for the velocities when spallation source terms are coupled.

The ratio of the source term vector ($\mathbf{S}_p V$) and residual vector ($\mathbf{R}$), as defined in Eqs. (11) and (4), respectively, is called the coupling term vector [25]. The absolute magnitudes of these elements determine the impact of the two-way coupling. A low absolute magnitude of these elements indicates that the corresponding coupling term does not affect the fluid. The presence of carbon species in the flow field is only due to the particle's surface reactions. The mass fluxes and the production rates of these species from the fluid side are negligibly small, thereby making the mass coupling terms high in magnitude. Hence, it can be seen from the above simulation that the carbon species produced by the particle affects the flow field by changing its composition. On the other hand, the momentum and energy fluxes of the fluid are higher when compared to the drag force and energy rate of the particle, making the momentum and energy coupling irrelevant. Similar behavior is also observed in the cases presented later in this paper. However, since the spallation phenomenon involves the ejection of thousands of particles whose combined source term is comparable to the flow field fluxes, a noticeable change to the temperature and dynamics of the gas mixture might become more apparent.

3.1.2. Air flow field

The mass removal of a spalled particle in an air environment occurs as a result of oxidation, nitridation and sublimation. The ejection parameters and physical time of the particle considered for this test case are shown in Table 6.

Table 6: Ejection parameters and physical time for single particle simulation in air environment

Size (μm)	Velocity (m/s)	Position (mm)	Angle (°)	Physical time (ms)
20	120	(0,10,0)	0	0.4580

To achieve time accuracy, the solution was computed with a time step size of 5×10^{-10} s, which corresponds to a maximum CFL of 0.625.

Figures 7, 8, 9, and 10 represent the simulation results of the mass coupling for the particle given in Table 6. These figures consist of temperature profiles and density profiles of CO, CN, C_1, C_2, and C_3 at different particle travel times. As opposed to the argon flow field, which only accounted for sublimation, the airflow field also includes oxidation and nitridation which depend on the concentrations of reaction species. The animation of this simulation is provided in the Supplementary Material.

Due to a high concentration of atomic oxygen and atomic nitrogen near the surface of the sample, the particle reacts and releases vapor soon after its ejection. However, the particle sublimates insignificantly due to its relatively low temperature. This behavior is shown in Fig. 7 at 0.10 ms of its travel time.

As the particle crosses the shock, at 0.20 ms of its travel, it starts to sublimate and release vapor of varying concentrations. The CO vapor's concentration decreases in the upstream region as atomic oxygen

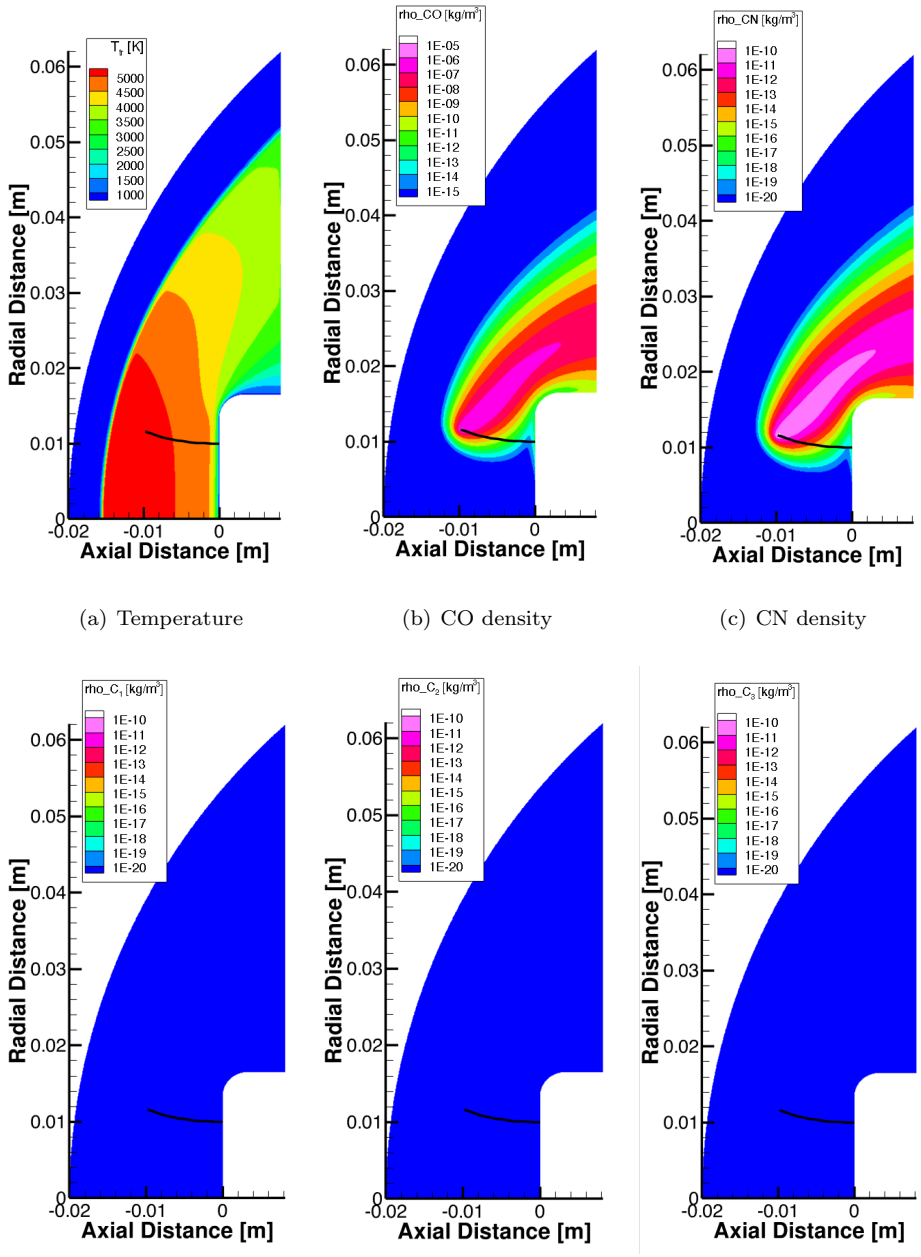

(a) Temperature (b) CO density (c) CN density

(d) C_1 density (e) C_2 density (f) C_3 density

Figure 7: Trajectory of the particle in a reacting air flow field at 0.10 ms with heterogeneous carbon reactions. (An animation of this figure is provided in the Supplementary Material.)

is nearly absent, and oxidation occurs only due to molecular oxygen. Also, the nitridation is minimal in the post-shock region due to nearly zero concentration of atomic nitrogen. Therefore, only a minuscule amount of CN vapor is produced as seen in Fig. 8.

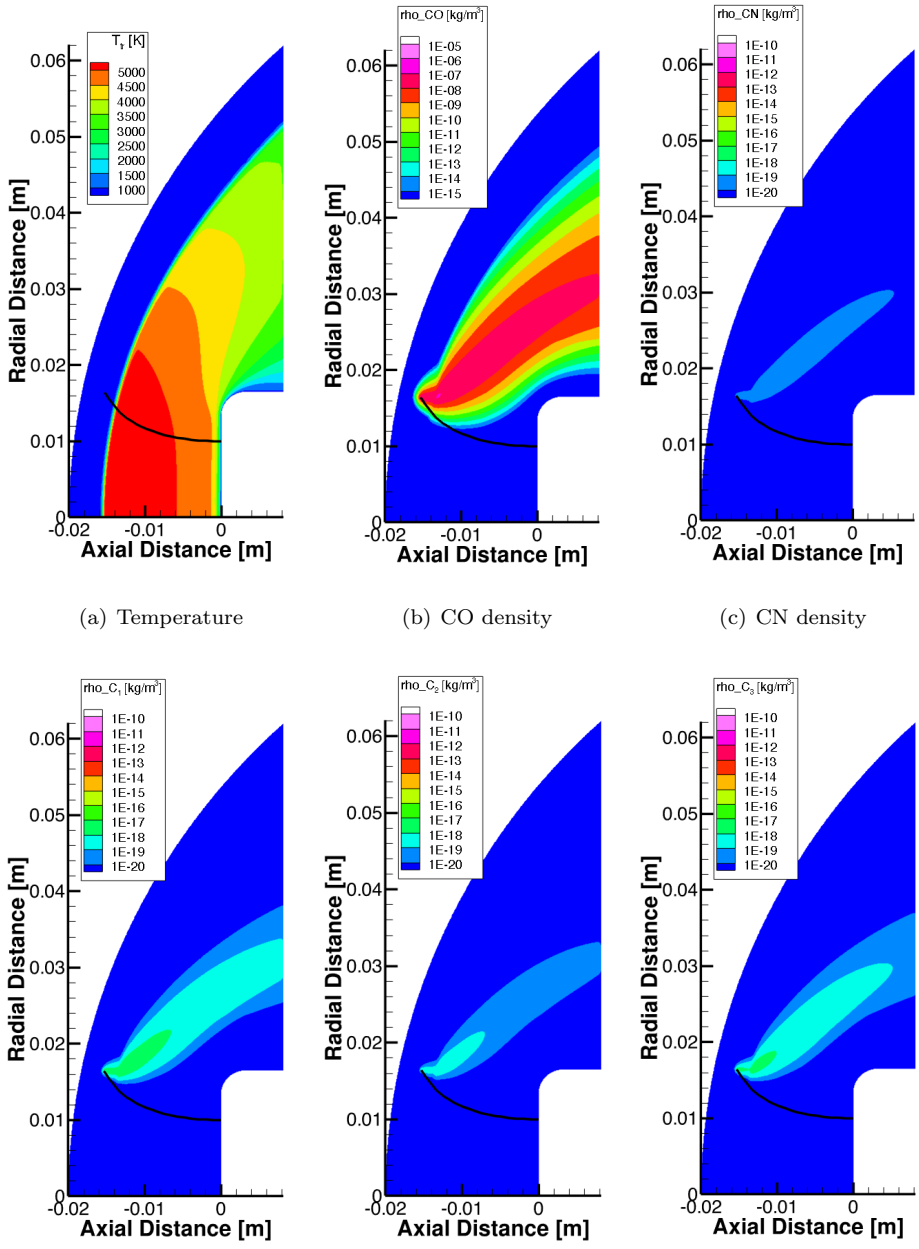

(a) Temperature (b) CO density (c) CN density

(d) C_1 density (e) C_2 density (f) C_3 density

Figure 8: Trajectory of the particle in a reacting air flow field at 0.20 ms with heterogeneous carbon reactions. (An animation of this figure is provided in the Supplementary Material.)

185 At 0.30 ms, the particle is still in the upstream region. As its temperature increases, the concentration of sublimate vapor increases. However, the concentrations of CO and CN vapor remain almost constant in this region. This behavior can be observed in Fig. 9.

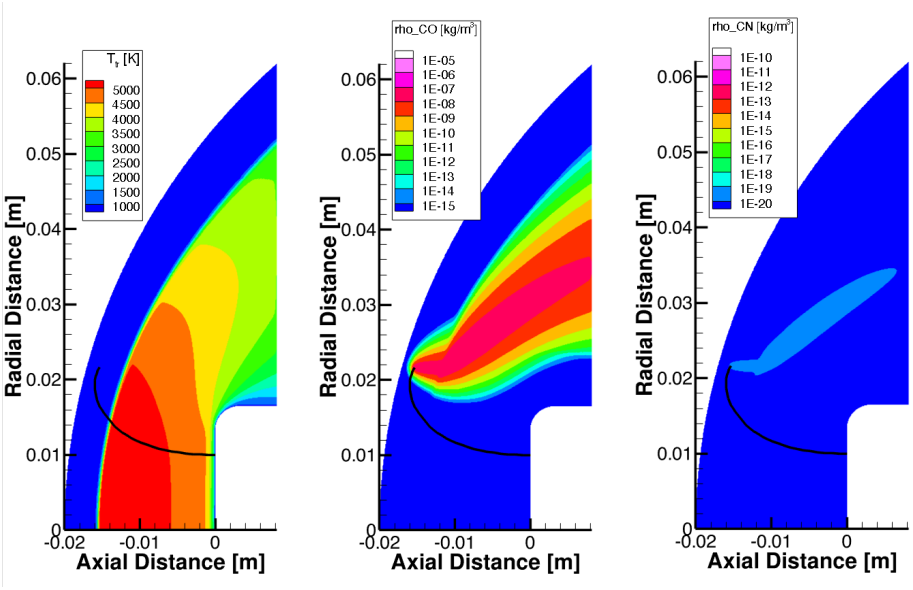

(a) Temperature (b) CO density (c) CN density

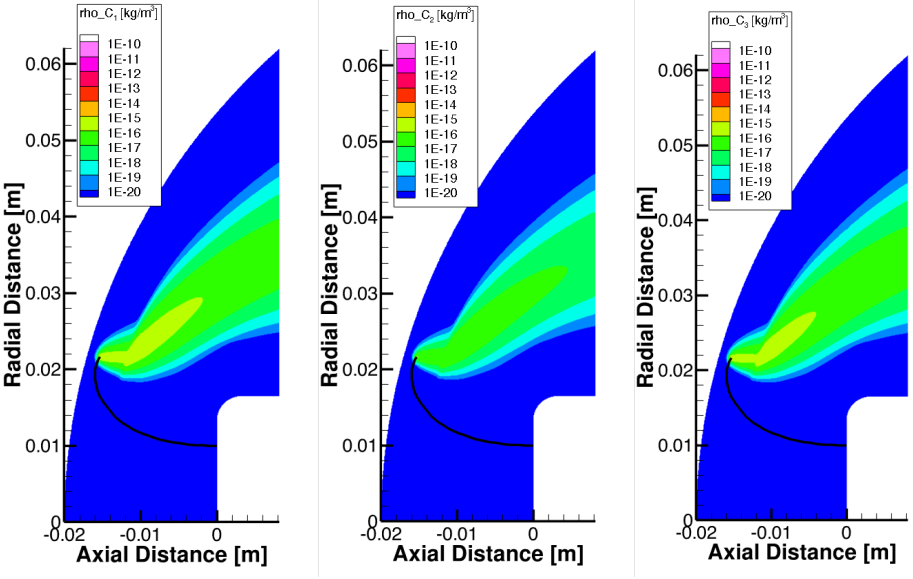

(d) C_1 density (e) C_2 density (f) C_3 density

Figure 9: Trajectory of the particle in a reacting air flow field at 0.30 ms with heterogeneous carbon reactions. (An animation of this figure is provided in the Supplementary Material.)

Figure 10 shows the particle after 0.44 ms of travel time. At that time, the particle is in the downstream region, and the amount of vapor released by oxidation, nitridation, and sublimation reactions increases.

From these figures (Figs. 7-10), it can be seen that the dominating species is CO, which is directly

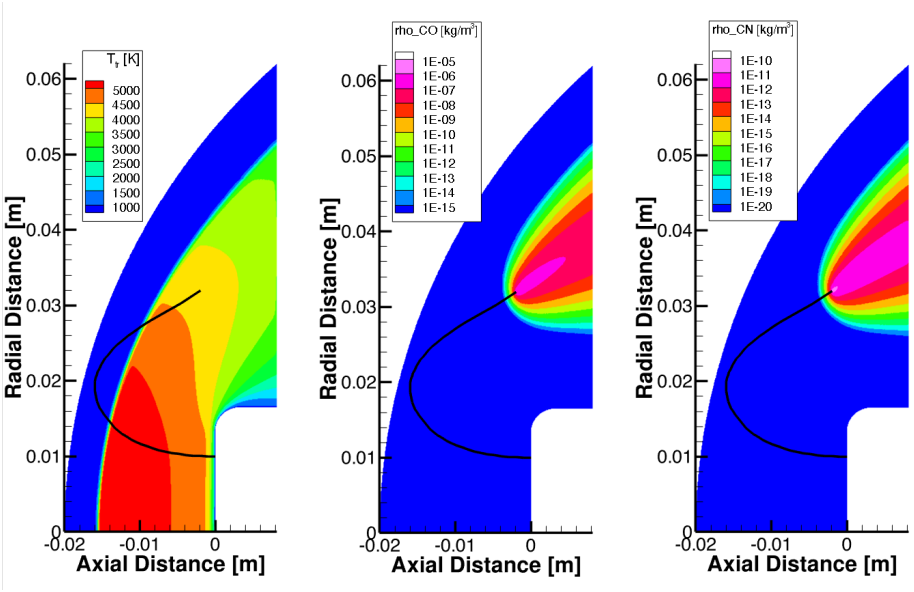

(a) Temperature (b) CO density (c) CN density

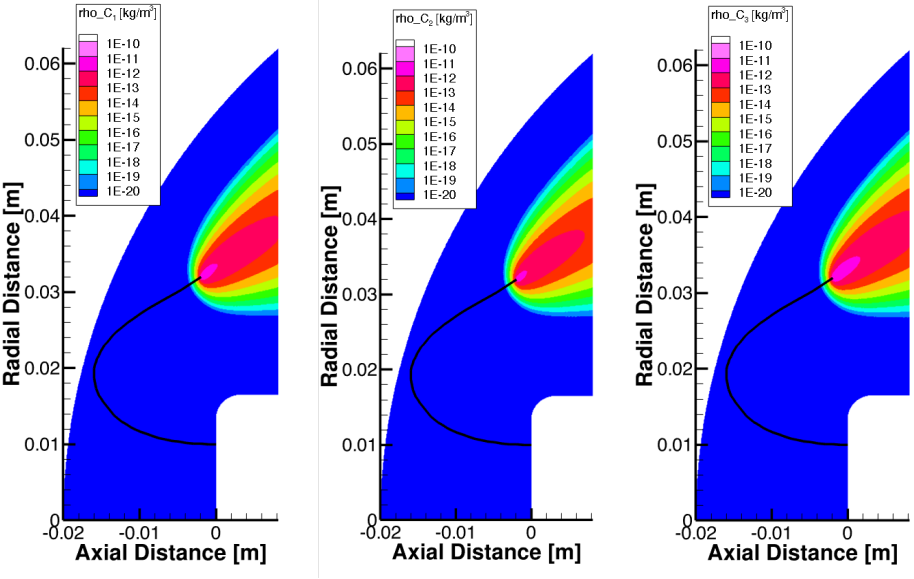

(d) C_1 density (e) C_2 density (f) C_3 density

Figure 10: Trajectory of the particle in a reacting air flow field at 0.44 ms with heterogeneous carbon reactions. (An animation of this figure is provided in the Supplementary Material.)

released as a result of oxidation. However, the spectroscopic experiments [7] observed high CN spectra in the upstream region. Since nitridation does not generate the amount of CN necessary to produce the observed quantities, other chemical processes must be present. It is hypothesized that the presence of CN is

due to the transformation of CO through a gas-phase exchange reaction [26, 27]:

$$\mathrm{CO} + \mathrm{N} \rightleftharpoons \mathrm{CN} + \mathrm{O} \tag{18}$$

In order to evaluate the conversion of CO to CN, this single equation is added to the flow field chemistry model of the CFD code, and the exact same simulation is performed again. Figure 11 compares the solutions of CN density profile when the exchange reaction given by Eq. 18 is considered or not.

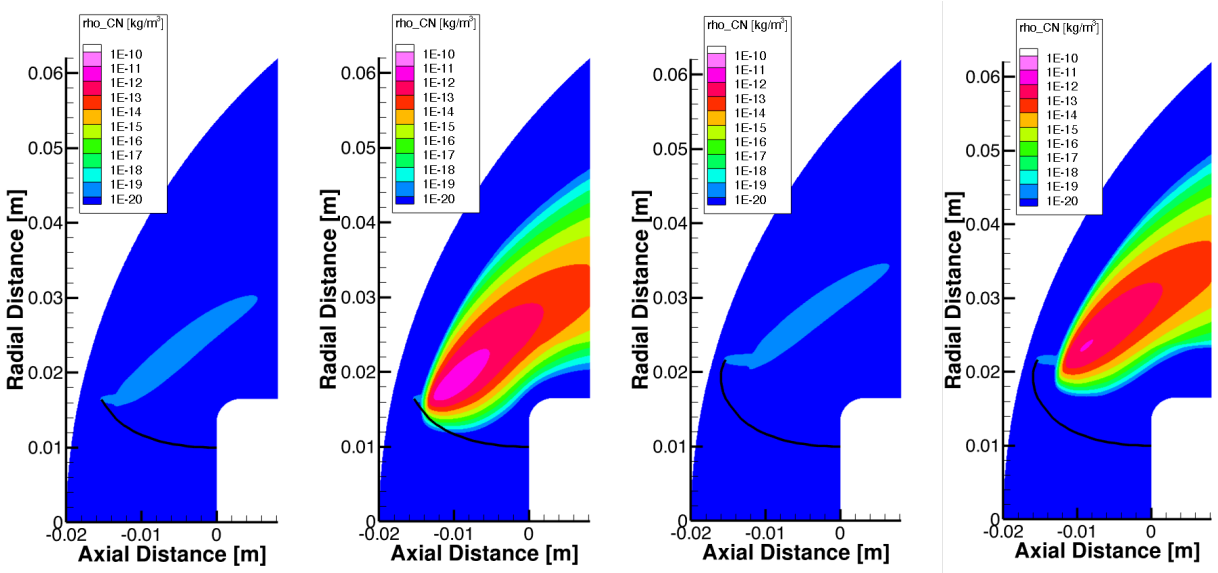

(a) CN density at 0.20 ms (without exchange reaction)

(b) CN density at 0.20 ms (with exchange reaction)

(c) CN density at 0.30 ms (without exchange reaction)

(d) CN density at 0.30 ms (with exchange reaction)

Figure 11: CN density profiles without and with the exchange reaction at 0.20 and 0.30 ms

Figures 11 (a) and 11 (b) represent the simulation of the particle at 0.20 ms of its travel time while Figs. 11 (c) and 11 (d) depict the simulation at 0.30 ms. Figures 11 (a) and (c) represent the CN density profile without adding the exchange reaction, which shows that the concentration of CN vapor released and subsequently diffused is very small. Figures 11 (b) and (d) illustrate the CN density profile when the exchange reaction is included. It is noted that there is a considerable amount of CN in the downstream region and very little in the upstream region. The CO vapor released by the particle within the shock is converted to CN. However, due to a very small concentration of N in the post-shock region, the exchange reaction is insignificant, and a very low concentration of CN is observed. It is, however, postulated that if more reactions are considered, more CN would be observed in the upstream region. Therefore, a list of dissociation and exchange gas-phase reactions [28] is added to the chemistry model of CFD, and listed in Table 7. It should be noted that the first three of the dissociation reactions and the first two of the exchange reactions were

already included in the earlier simulation (Figs. 7-10). The reactions involving carbon products are the ones that are added for this simulation. The simulation with same ejection parameters as given in Table 6 are used to understand the effects of additional chemistry, and the results are shown in Figures 12, 13, 14, and 15. The animation of this simulation is provided in the Supplementary Material.

Table 7: Dissociation and exchange reactions considered for single particle simulation in air environment

Type	Reactions
Dissociation Reactions	$N_2 + M \rightleftharpoons 2\,N + M$
	$O_2 + M \rightleftharpoons 2\,O + M$
	$NO + M \rightleftharpoons N + O + M$
	$C_2 + M \rightleftharpoons C_1 + C_1 + M$
	$CN + M \rightleftharpoons C_1 + N + M$
	$CO + M \rightleftharpoons O + C_1 + M$
Exchange Reactions	$N_2 + O \rightleftharpoons NO + N$
	$NO + O \rightleftharpoons O_2 + N$
	$CO + N \rightleftharpoons CN + O$
	$C_1 + N_2 \rightleftharpoons CN + N$
	$C_1 + NO \rightleftharpoons CN + O$
	$C_1 + NO \rightleftharpoons CO + N$
	$C_1 + O_2 \rightleftharpoons O + CO$
	$C_2 + C_2 \rightleftharpoons C_3 + C_1$
	$C_2 + N_2 \rightleftharpoons CN + CN$
	$CN + C_1 \rightleftharpoons C_2 + N$

At 0.10 ms of the particle's travel time, the added reactions increase the concentration of C_1 as seen in Fig. 12 (d) in spite of the temperature being low. Since half of the dissociation reactions produce C_1, it is believed that these may be responsible for an increase in C_1 concentration. Figure 12 also shows the other products' density profiles as a result of particle's oxidation, nitridation, and sublimation (C_2 and C_3) which

closely resemble the earlier simulation shown in Fig. 7.

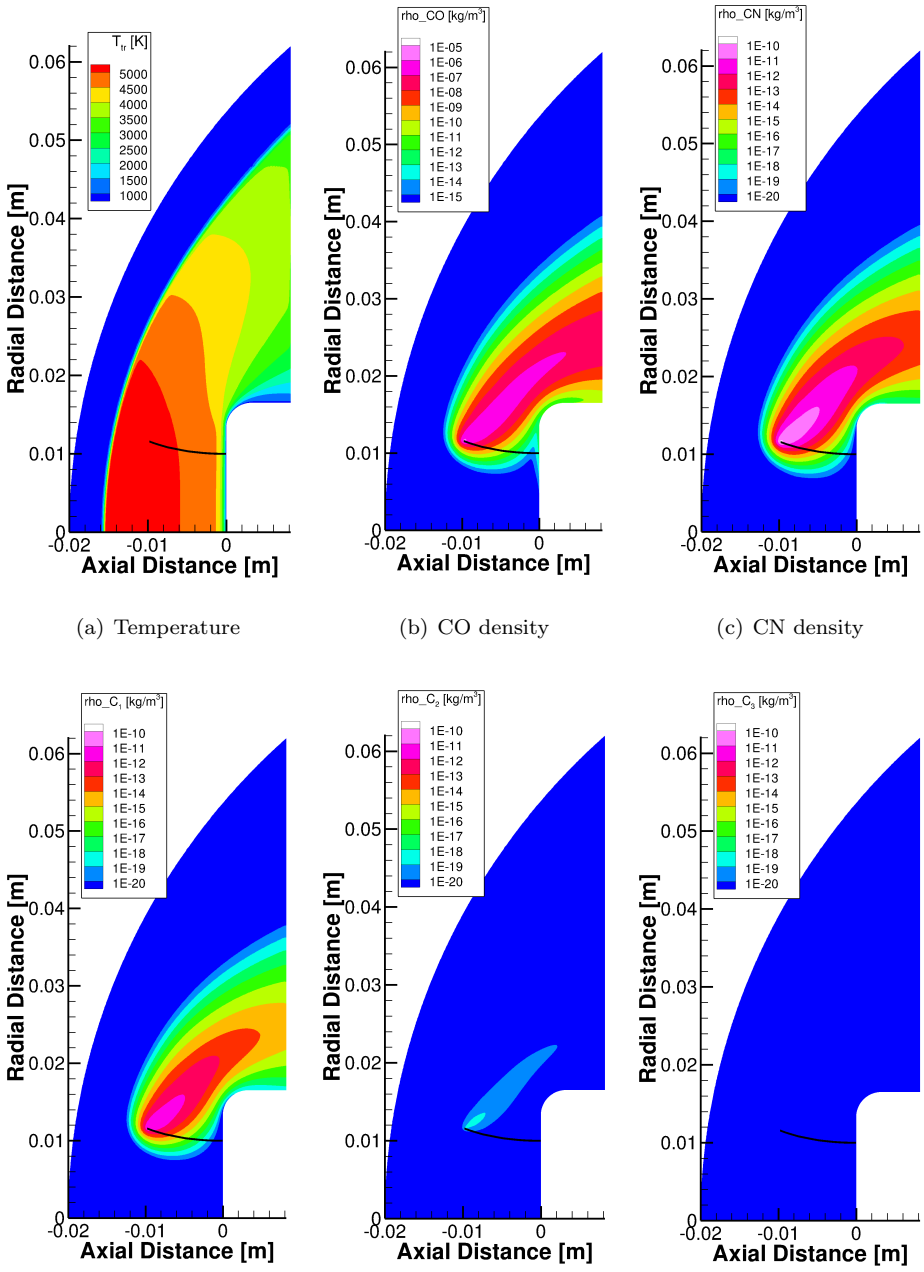

(a) Temperature (b) CO density (c) CN density

(d) C_1 density (e) C_2 density (f) C_3 density

Figure 12: Trajectory of the particle in a reacting air flow field at 0.10 ms with heterogeneous and homogeneous carbon reactions. (An animation of this figure is provided in the Supplementary Material.)

When the particle crosses the shock at 0.20 ms, a change in the C_1 and CN concentrations is observed in

both upstream and downstream locations. However, the change in CN density profile is similar to what was observed in Fig. 11 (b). While comparing with Fig. 8, the only significant dissociation reactions are the ones in which C_2 and CO are converted to C_1 vapor. The sublimate vapor further undergoes exchange reactions to produce more of CN and C_1 which can be seen in Fig. 13. The other concentrations remain unchanged with minimal effect from added chemical reactions.

At 0.30 ms of particle's travel time, there is a further increase in the C_1 and CN concentration in both upstream and downstream of the shock. It should be noted that when compared to the CN concentration as seen in Fig. 11 (d), the added reactions produce more CN. It can be inferred that the presence of CN in the upstream region of the shock, as observed from the spectroscopic experimental data [7], is indeed due to the additional gaseous phase reactions between carbon products and air. The oxidation and sublimation of the particle undergo similar changes when compared with Fig. 9. The above-mentioned behavior can be observed in Fig. 14.

At 0.44 ms of its travel as shown in Fig. 15, the particle enters the downstream region with higher CO, C_2, and C_3 concentrations, and lower CN and C_1 concentrations when compared to Fig. 10. It is believed that the exchange reactions involving C_1 and CN play a significant role in this region.

These results indicate that along the particle's path, their chemistry in conjunction with the gas-phase reactions increases the concentration of carbon products which could not be explained by other ablative phenomena.

Similar to the argon environment, when the mass and energy coupling and the total coupling results are compared to only mass coupling simulation results, they appear virtually identical: the temperature is different by nearly 0.01 K when spallation source terms are applied.

From these single-particle simulation results, it can be seen that the particle releases vapor in both upstream and downstream regions. This reinforces the hypothesis that the presence of spalled particles ahead of the shock is the reason for the optical emissions of the carbon species observed in that region.

The conclusions in this section are based on the simulation of one particular trajectory of one particle. The trajectory of the particle is a function of its size and ejection parameters. In order to assess the effect of the particle on the flow field, a parametric study on the parameters that affect the particle's motion is conducted.

3.1.3. Parametric study

The parametric study is performed by varying each parameter while keeping others constant. The objective of this study is to summarize the effect of the particle's behavior on the flow field by including all parameters that affect its motion. The study is conducted in a Mach 5 air environment where the total density of the carbon products released by the particle is considered. A baseline case for simulation is used and other simulations where each parameter is changed are compared to the baseline case. The results

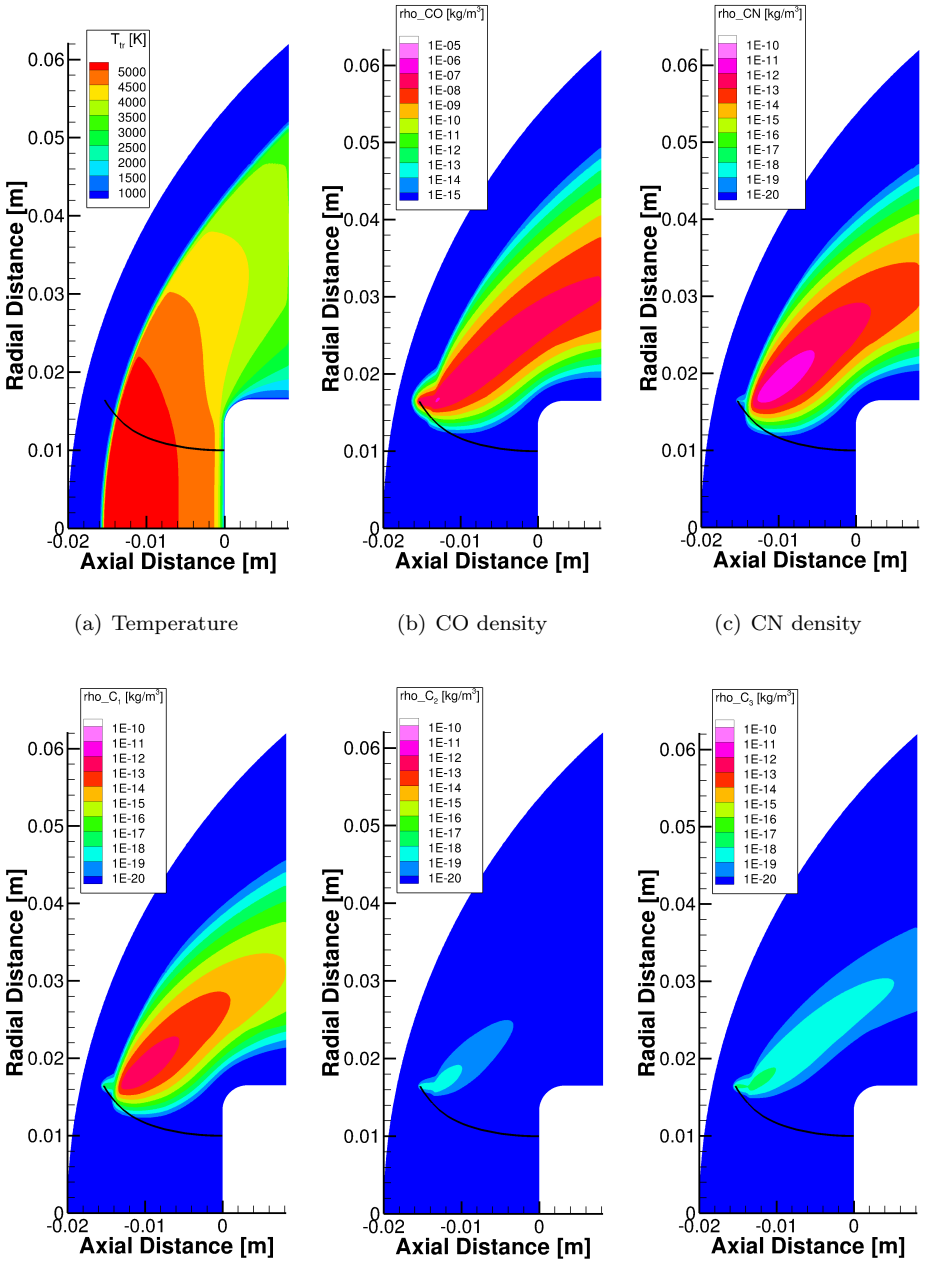

(a) Temperature (b) CO density (c) CN density

(d) C_1 density (e) C_2 density (f) C_3 density

Figure 13: Trajectory of the particle in a reacting air flow field at 0.20 ms with heterogeneous and homogeneous carbon reactions. (An animation of this figure is provided in the Supplementary Material.)

are compared at the same timestamps since the simulation is transient in nature. The initial parameters and total physical time for simulation considered as the baseline case for the parametric study are given in

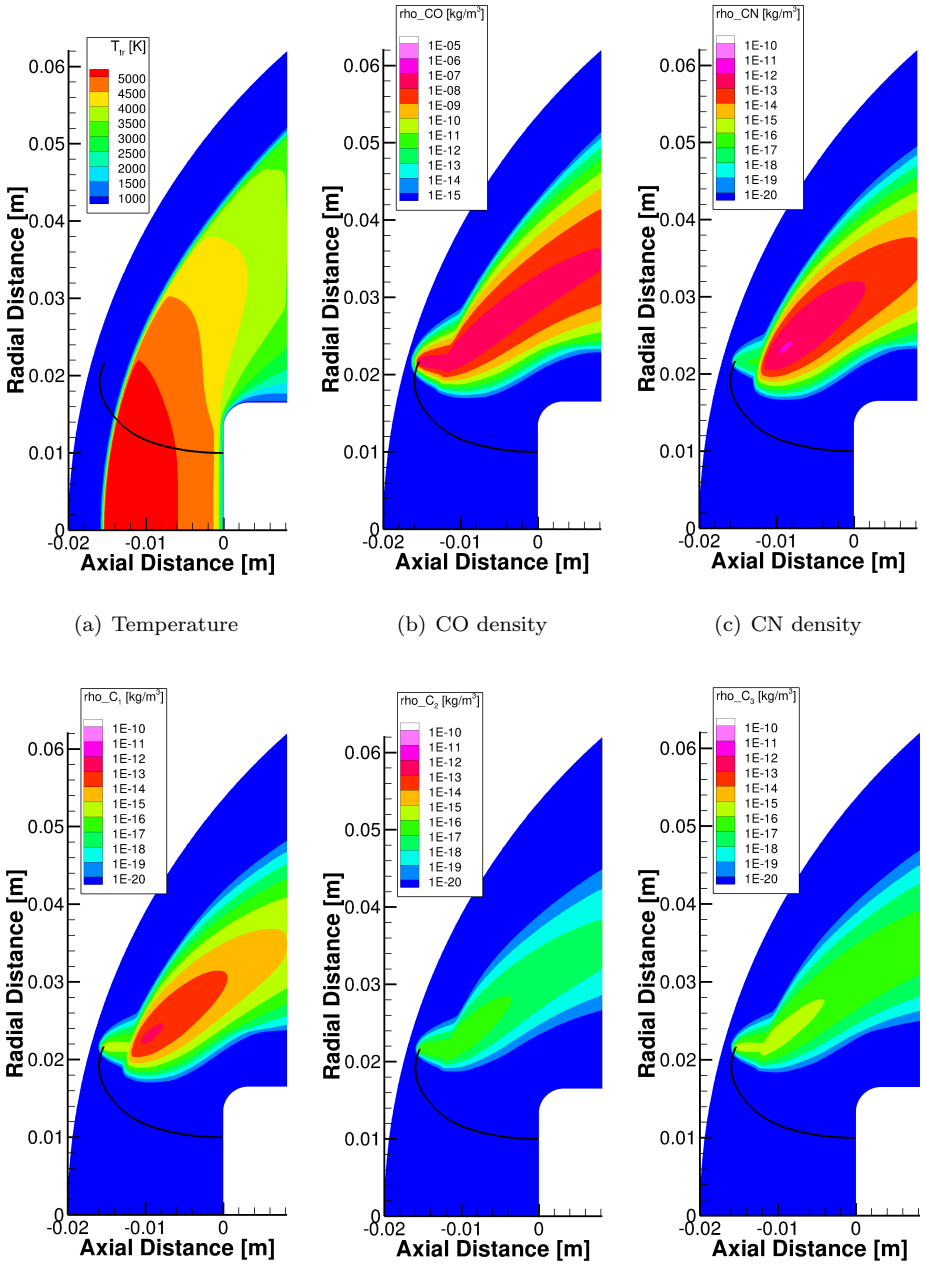

(a) Temperature (b) CO density (c) CN density

(d) C_1 density (e) C_2 density (f) C_3 density

Figure 14: Trajectory of the particle in a reacting air flow field at 0.30 ms with heterogeneous and homogeneous carbon reactions. (An animation of this figure is provided in the Supplementary Material.)

Table 8 and the simulation results are shown in Fig. 16. All the simulations considered for the parametric study were computed with a time step size of 8×10^{-10} s, which corresponds to the maximum CFL of 1.00.

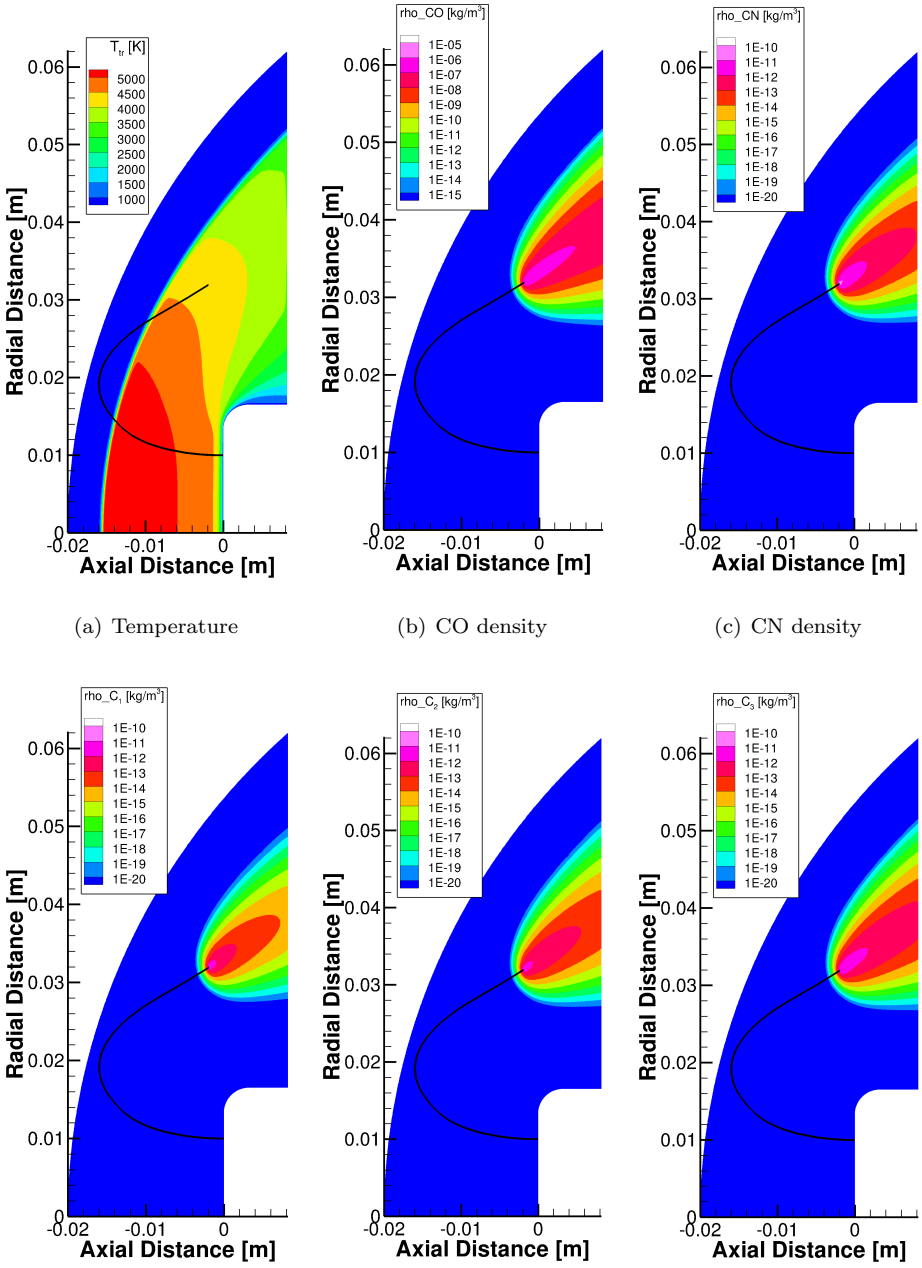

(a) Temperature (b) CO density (c) CN density

(d) C_1 density (e) C_2 density (f) C_3 density

Figure 15: Trajectory of the particle in a reacting air flow field at 0.44 ms with heterogeneous and homogeneous carbon reactions. (An animation of this figure is provided in the Supplementary Material.)

The simulation of the baseline case shows the particle's path at 0.10 ms, as it travels towards the shock and releases carbon vapor soon after the ejection. As the particle crosses the shock at 0.20 ms, there is a

Table 8: Ejection parameters and physical time of baseline case for parametric study

Size (μm)	Velocity (m/s)	Position (mm)	Angle (°)	Physical time (ms)
24	100	(0,10,0)	0	0.5651

decrease in C density profile. The concentration of C is increased again as the particle enters the shock area as observed at 0.44 ms. The complete trajectory of the particle is presented over the temperature contour of the flow field in Fig. 16 (a). The chemical behavior of the particle is similar to the one discussed in Section 3.1.2.

Variation of particle size. A time-accurate solution is computed by varying only particle size while other parameters are kept constant. The ejection parameters and total physical time for the simulation are given in Table 9.

Table 9: Ejection parameters and physical time for parametric study with variation of size

Size (μm)	Velocity (m/s)	Position (mm)	Angle (°)	Physical time (ms)
20	100	(0,10,0)	0	0.4624

The result of the above simulation is shown in Fig. 17. It should be noted that due to the decrease in size and thus reduced inertia, the particle interacts with the shock but does not cross it. Compared to Fig. 16, there is an overall increase in the released carbon vapor by the particle. The particle travels through temperature gradients in the downstream region of the shock which causes an increase in its temperature and more surface recession. However, the particle's total physical time to pass through the computational domain is less when compared to the baseline case. Therefore, comparing at 0.44 ms is not possible. Instead, the simulation at 0.32 ms is presented in Fig. 17 (e), before it exits the computational domain.

Variation of ejection velocity. The ejection velocity is changed and a time-accurate solution is computed. The ejection parameters and total physical time for the simulation are given in Table 10 and the simulation results in Fig. 18.

Table 10: Ejection parameters and physical time for parametric study with variation of ejection velocity

Size (μm)	Velocity (m/s)	Position (mm)	Angle (°)	Physical time (ms)
24	75	(0,10,0)	0	0.3075

The results show a similar behavior to the study conducted by changing the size of the particle. With low ejection velocity, the particle travels through the downstream region of the shock. The path through

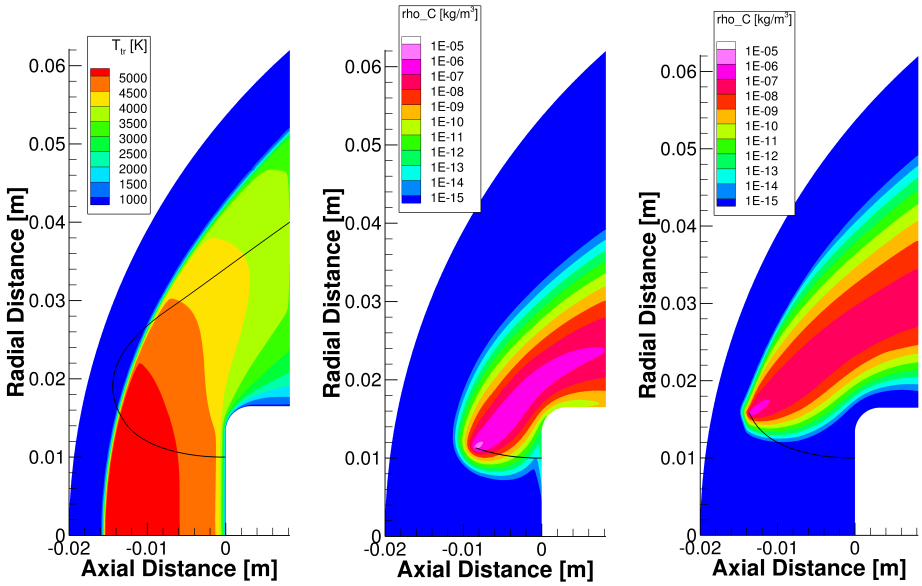

(a) Temperature (b) C density at 0.10 ms (c) C density at 0.20 ms

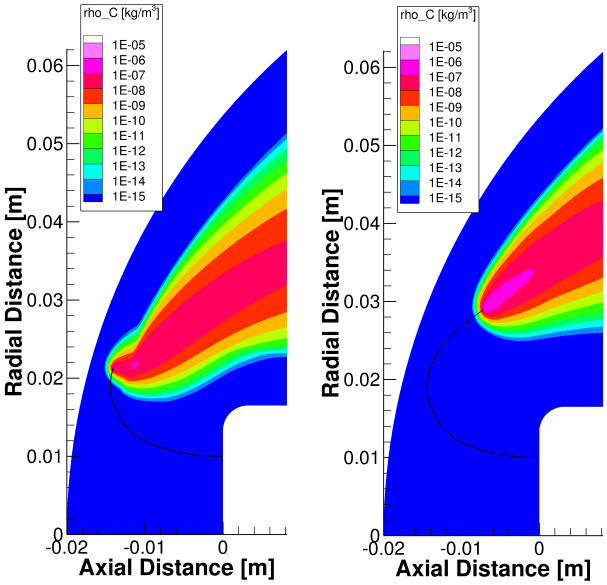

(d) C density at 0.30 ms (e) C density at 0.44 ms

Figure 16: Trajectory of the particle in an air flow field for baseline case

high-temperature regions allows the particle to react more and release more carbon vapor which can be observed in Fig. 18. The particle's behavior is not compared at 0.44 ms as it exits the computational domain well before that time.

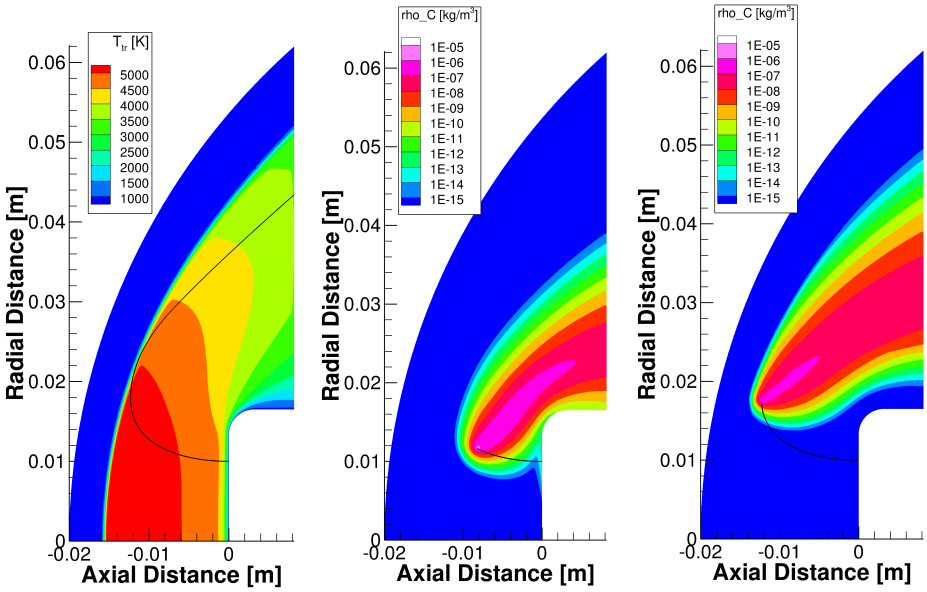

(a) Temperature (b) C density at 0.10 ms (c) C density at 0.20 ms

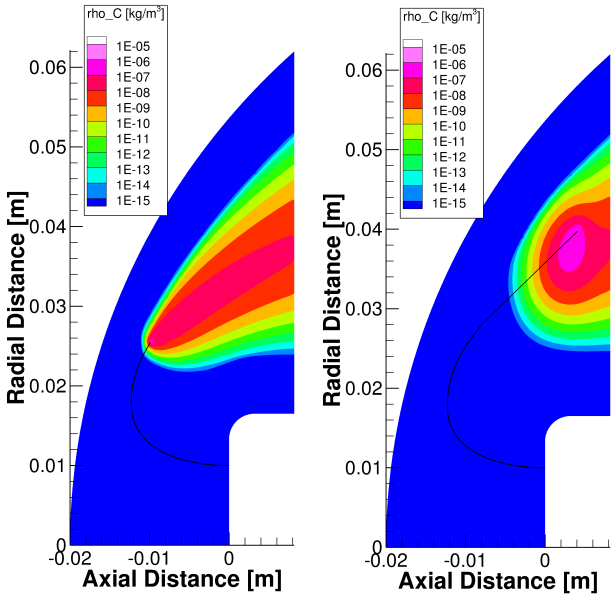

(d) C density at 0.30 ms (e) C density at 0.32 ms

Figure 17: Trajectory of the particle in an air flow field for 20 µm particle (other ejection parameters same as baseline case).

Variation of ejection position. The ejection parameters and total physical time for the time accurate simulation where the ejection position is varied are presented in Table 11.

The results of the simulation are illustrated in Fig. 19. The trajectory of the particle crosses the shock

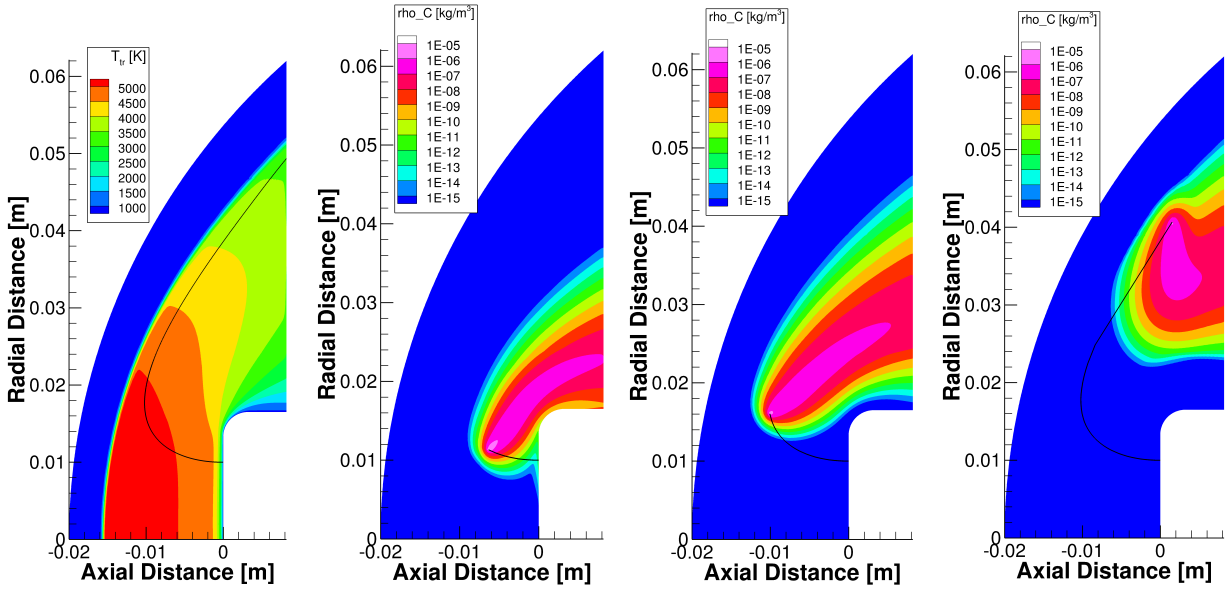

(a) Temperature (b) C density at 0.10 ms (c) C density at 0.20 ms (d) C density at 0.30 ms

Figure 18: Trajectory of the particle in an air flow field for ejection velocity of 75 m/s (other ejection parameters same as baseline case)

Table 11: Ejection parameters and physical time for parametric study with variation of ejection position

Size (μm)	Velocity (m/s)	Position (mm)	Angle (°)	Physical time (ms)
24	100	(0,5,0)	0	0.6137

for this case. In comparison with Fig. 16, it can be seen that the particle releases a large amount of carbon with diffused vapor also traveling towards the center-line direction. The temperature of the fluid and concentrations of atomic oxygen and nitrogen increase as the position moves towards the centerline. The particle's chemical reactivity increases when it is ejected from the positions that are closer to the centerline. Also, with the bulk velocity of the fluid being low at this position, the released carbon vapor is diffused along the downstream region of the shock and around the sample.

Variation of ejection angle. For this case, three different time-accurate solutions with different ejection angles are considered and their details are given in Table 12.

The simulation results for ejection angle 30°, 60°, and 90° are presented in Fig. 20, 21, and 22, respectively. The particle with an ejection angle of 30° passes through the shock and travels through the upstream region until it exits the computational domain. Based on the trajectory and in comparison to Fig. 16, it can be seen that the density profile of C released by the particle increases as it travels towards the shock and goes

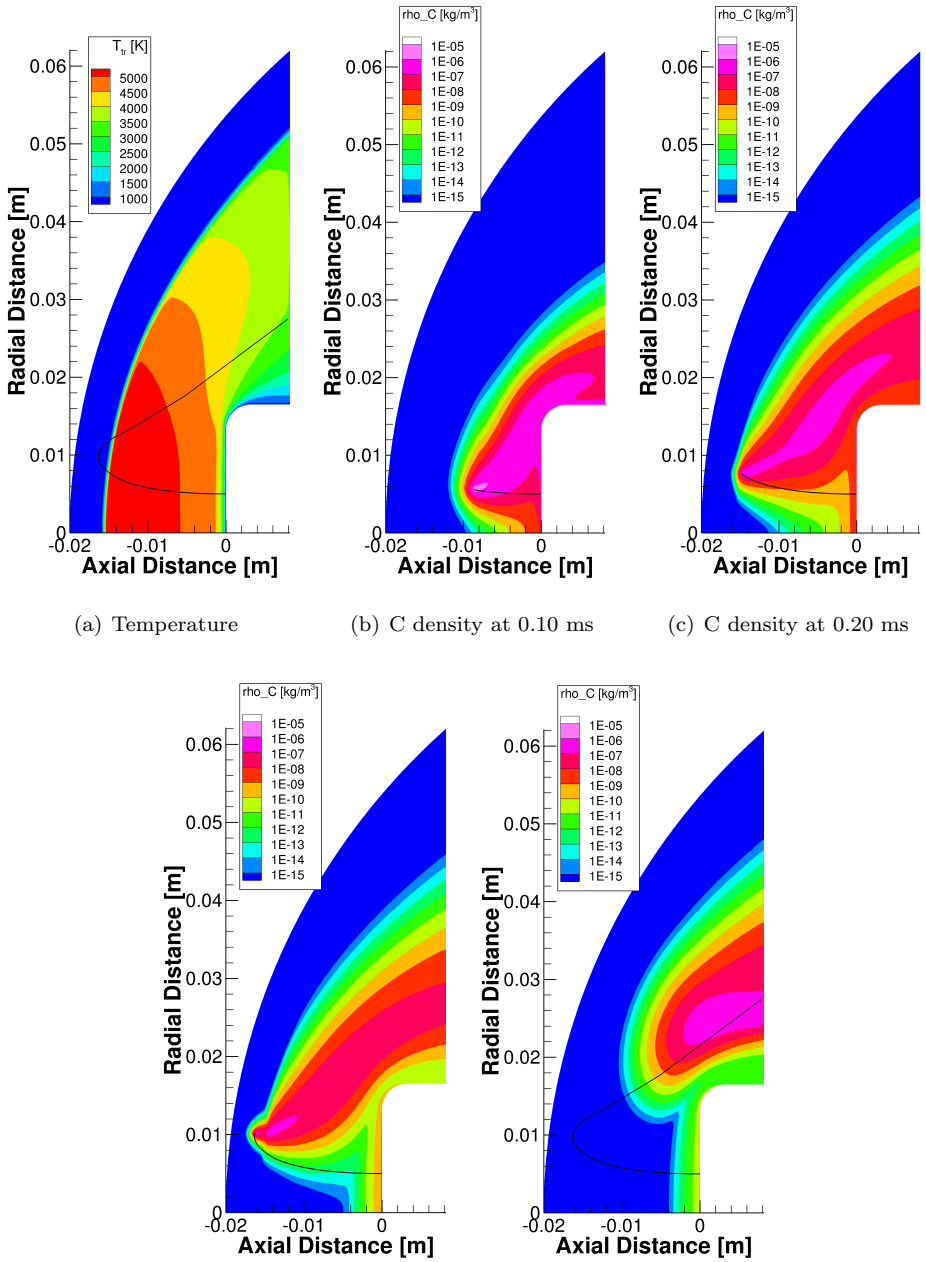

(a) Temperature (b) C density at 0.10 ms (c) C density at 0.20 ms

(d) C density at 0.30 ms (e) C density at 0.44 ms

Figure 19: Trajectory of the particle in an air flow field for ejection position at $(0, 5, 0)$ (other ejection parameters same as baseline case)

on to decrease thereafter. This behavior of the particle can be seen in Fig. 20.

The path of the particle ejected at an angle of 60° is similar to that of a particle ejected at an angle of 30° as seen in Fig. 21. However, the particle passes through lower temperature zones when compared to that

Table 12: Ejection parameters and physical time for parametric study with variation of ejection position

Size (μm)	Velocity (m/s)	Position (mm)	Angle (°)	Physical time (ms)
24	100	(0,10,0)	30	0.4748
24	100	(0,10,0)	60	0.3303
24	100	(0,10,0)	90	0.2199

of the 30° angle trajectory. The density profile of C increases as the particle moves towards the shock and decreases as it travels through the upstream region. The comparison to 0.44 ms travel time is not performed as the particle exits the computational domain before that time.

In the case of the ejection angle 90° as shown in Fig. 22, the particle travels through the downstream region of the shock and exits the computational domain in a very short time. With the low bulk velocity of the fluid near the sample, the released carbon vapor from the particle is diffused along the downstream region and around the sample. The concentration of the released vapor keeps increasing until it exits the domain.

The parametric study conducted indicates that the closer the ejection position of the particle to the center-line, the greater the chemical reactivity of the particle and hence, larger amount of vapor released. With the decrease in mass and ejection velocity, the particle tends to travel through the downstream region and does not cross the shock, thereby, releasing more vapor. In addition, the particle's reactivity increases and the particle releases more vapor with decrease in ejection angle from 90° to 0°.

3.2. Multiple particles simulation

In this section, the same process described earlier is repeated, but more than one particle is ejected in the flow field at the same time.

3.2.1. Argon flow field

The ejection parameters and physical time of the particles considered for multiple particle simulations are given in Table 13.

Table 13: Ejection parameters and physical time for multiple particles simulation in argon environment

Size (μm)	Velocity (m/s)	Position (mm)	Angle (°)	Physical time (ms)
12	380	(0,10,0)	0	0.2370
14	370	(0,13,0)	0	0.2697
16	360	(0,07,0)	0	0.3323

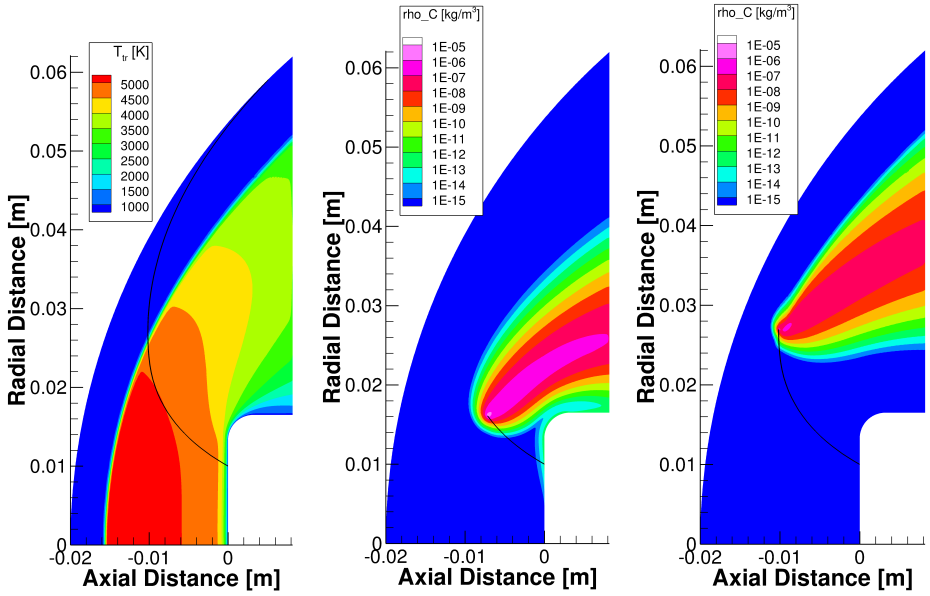

(a) Temperature (b) C density at 0.10 ms (c) C density at 0.20 ms

(d) C density at 0.30 ms (e) C density at 0.44 ms

Figure 20: Trajectory of the particle in an air flow field for 30° ejection angle (other ejection parameters same as baseline case)

Figures 23, 24, 25, and 26 illustrate the multiple particles simulation in an argon flow field at different travel times. The simulation was performed at a time step size of 4×10^{-9} s, corresponding to a maximum CFL of 0.824, which ensures time accuracy. The animation of this simulation is provided in the Supplementary

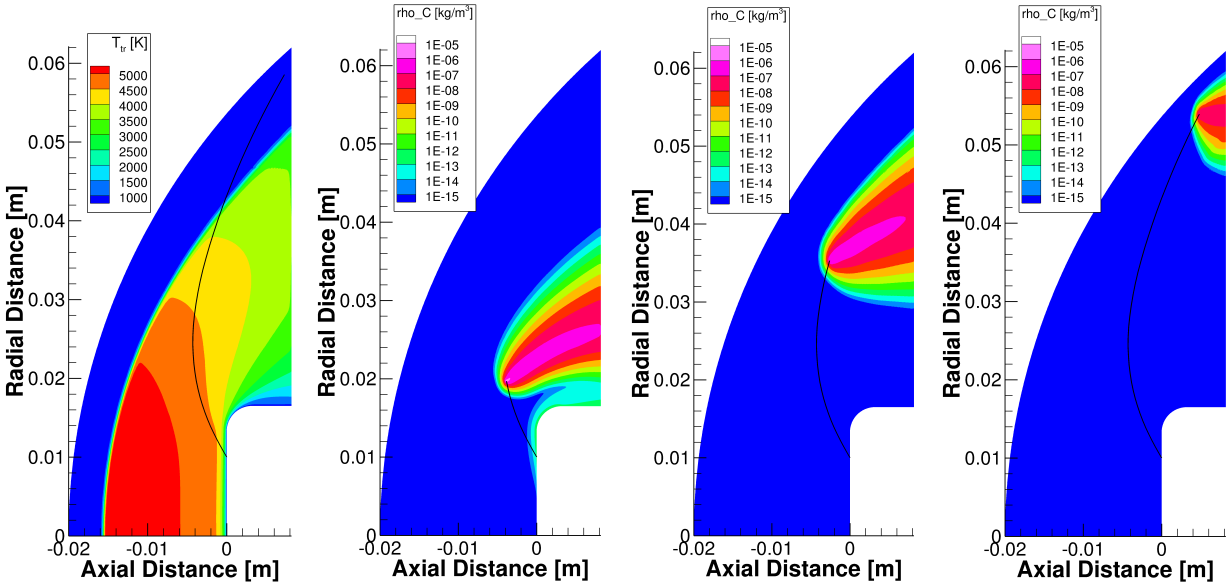

(a) Temperature (b) C density at 0.10 ms (c) C density at 0.20 ms (d) C density at 0.30 ms

Figure 21: Trajectory of the particle in an air flow field for 60° ejection angle (other ejection parameters same as baseline case)

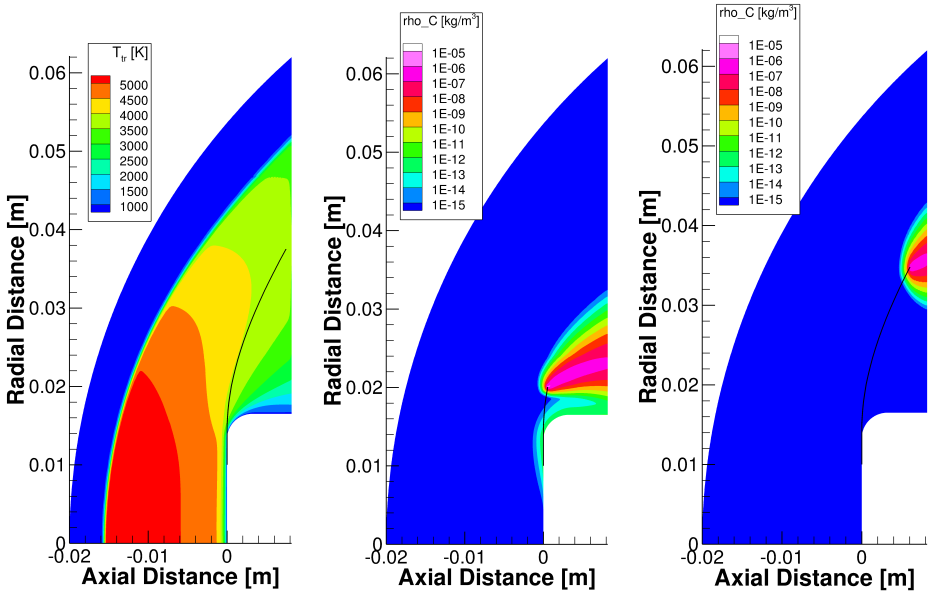

(a) Temperature (b) C density at 0.10 ms (c) C density at 0.20 ms

Figure 22: Trajectory of the particle in an air flow field for 90° ejection angle (other ejection parameters same as baseline case)

Material.

The behavior of the particles is similar to the results observed for the single particle simulation. At 70 µs from ejection, the particles approach the shock. With their temperatures being relatively low, they show negligible signs of recession, as seen in Fig. 23.

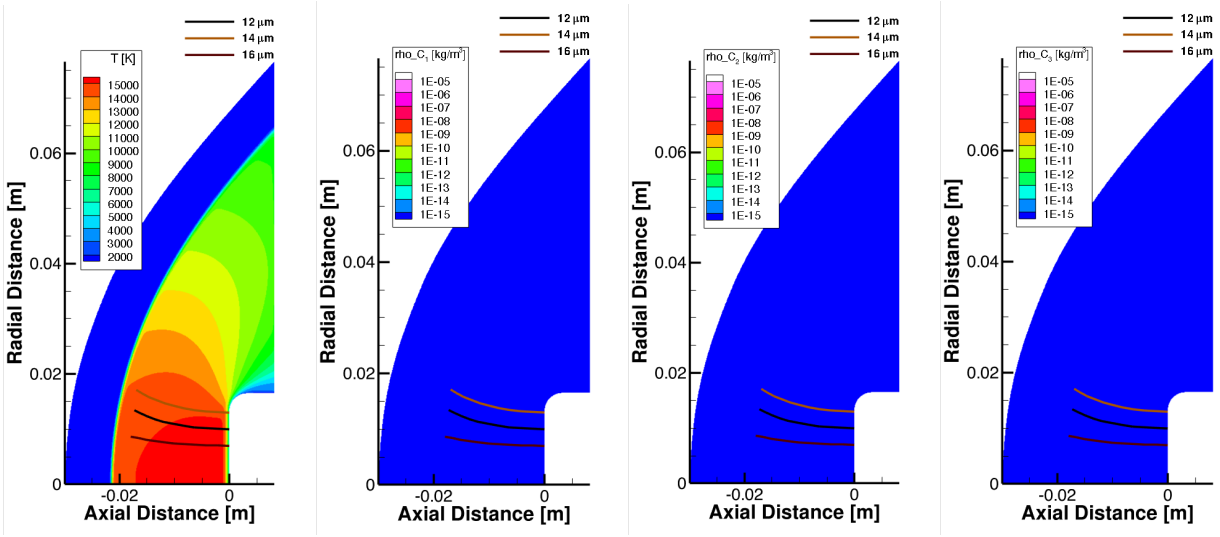

(a) Temperature (b) C_1 density (c) C_2 density (d) C_3 density

Figure 23: Trajectories of the particles in an argon flow field at 0.07 ms with heterogeneous carbon reactions. (An animation of this figure is provided in the Supplementary Material.)

The particles tend to sublimate in the post-shock region (0.15 ms of travel time), releasing different vapor concentrations. The vapor then convects and diffuses in a much larger region downstream, as seen in Fig. 24.

At a travel time of 0.23 ms, two of the particles re-enter the shock region as shown in Fig. 25. The concentrations of the carbon vapor released increase significantly and propagate to a much larger area.

As soon as these two particles complete their travel in the computational domain, the diffused vapor area decreases and the contribution only comes from the third particle, as shown in Fig. 26.

It is noticed that even with multiple spalled particles in the flow field, the temperature changes by a maximum of only 0.1 K. The other parameters remain the same throughout the simulation.

3.2.2. Air flow field

The ejection parameters for the particles simulated in this section are given in Table 14. The solution is computed at a time step size of 8×10^{-10} s, which corresponds to a maximum CFL of 1.000 to maintain time accuracy.

The particles of size 20 µm, 25 µm, and 30 µm penetrate through the shock, whereas the 15 µm does

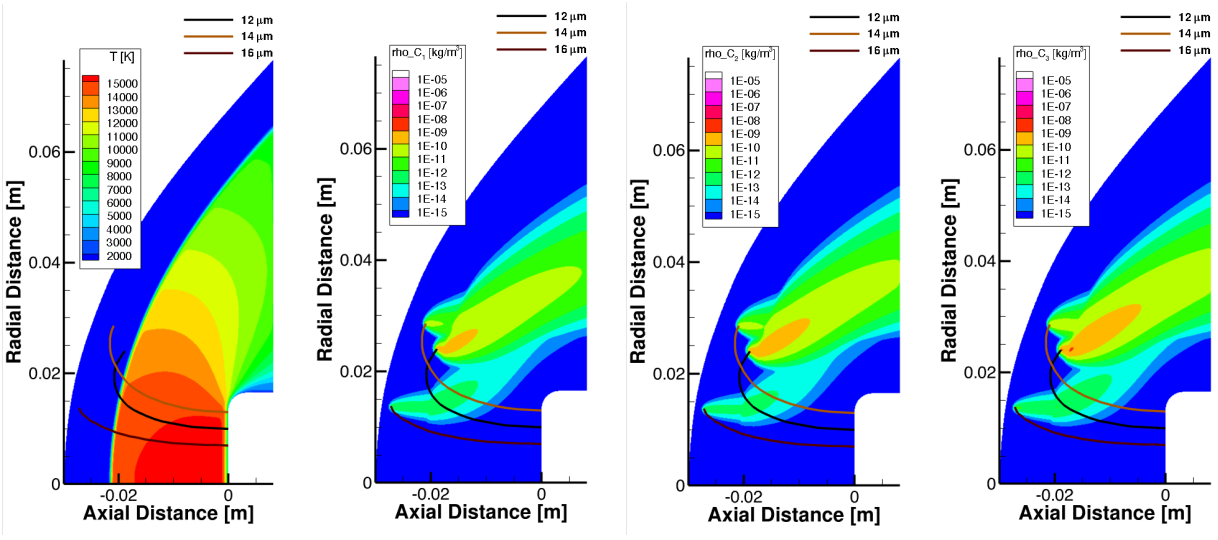

(a) Temperature (b) C_1 density (c) C_2 density (d) C_3 density

Figure 24: Trajectories of the particles in an argon flow field at 0.15 ms with heterogeneous carbon reactions. (An animation of this figure is provided in the Supplementary Material.)

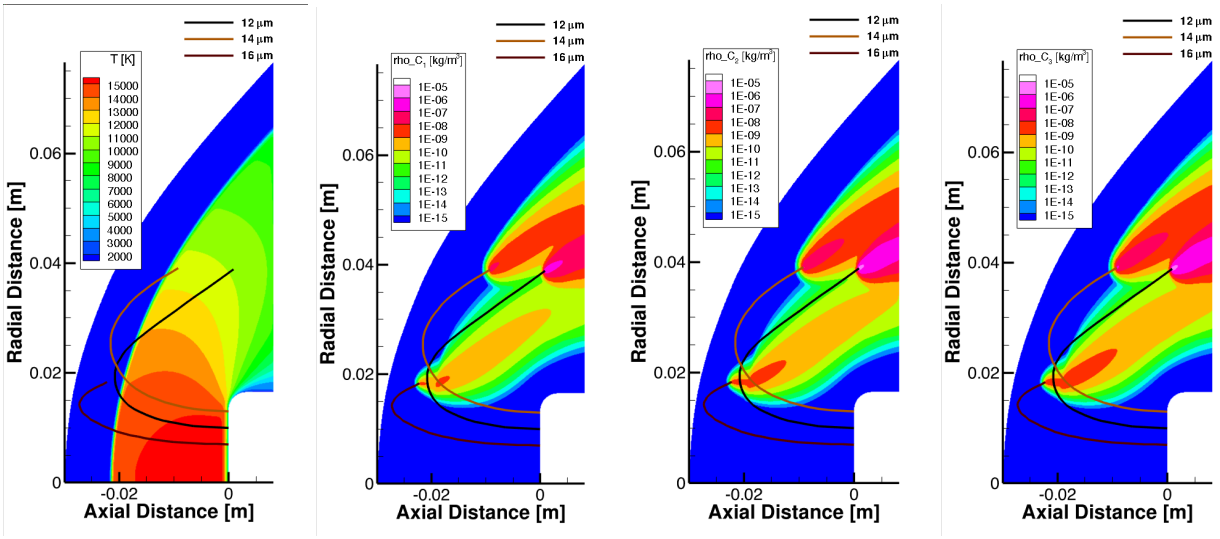

(a) Temperature (b) C_1 density (c) C_2 density (d) C_3 density

Figure 25: Trajectories of the particles in an argon flow field at 0.23 ms with heterogeneous carbon reactions. (An animation of this figure is provided in the Supplementary Material.)

not. The behaviors of these particles are shown in Figs. 27, 28, 29, and 30 at the respective times. The animation of this simulation is provided in the Supplementary Material.

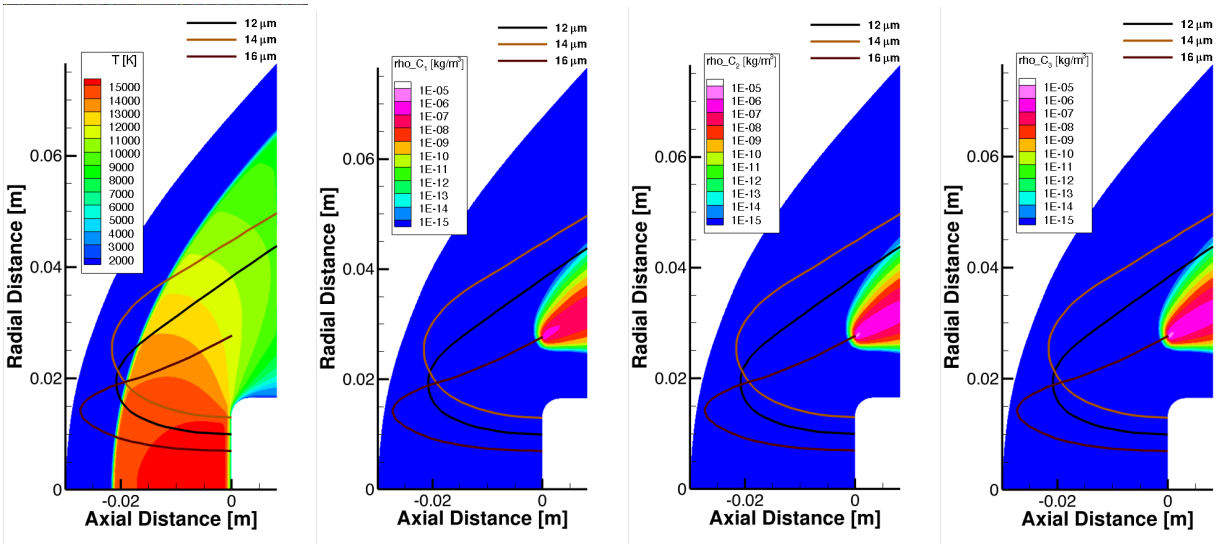

(a) Temperature (b) C_1 density (c) C_2 density (d) C_3 density

Figure 26: Trajectories of the particles in an argon flow field at 0.33 ms with heterogeneous carbon reactions. (An animation of this figure is provided in the Supplementary Material.)

Table 14: Ejection parameters and physical time for multiple particles simulation in air environment

Size (µm)	Velocity (m/s)	Position (mm)	Angle (°)	Physical time (ms)
15	70	(0,05,0)	0	0.1866
20	120	(0,10,0)	0	0.4580
25	100	(0,13,0)	0	0.5590
30	85	(0,08,0)	0	0.5744

At 0.09 ms, the particles start producing large concentrations of CO and CN vapors. However, the particles hardly sublimate as their temperatures are relatively low. The simulation at this time is illustrated in Fig. 27. The released vapor is seen to diffuse over a larger area and also observed to diffuse towards the center-line direction.

Figure 28 shows the simulation at 0.19 ms. At this time, the 20 µm particle passes through the shock, the 25 µm particle nearly comes close to the shock, and the 30 µm particle is still traveling towards the shock. The 15 µm particle, however, has already changed direction while in the high temperature region and will never reach the shock. The contribution to the CO vapor density decreases for particles that cross the shock and remains almost the same for the particles that are in the downstream region. Similarly, the particles that cross the shock generate very little CN vapor while the other particles contribute moderately. The 15 µm particle starts sublimating, and since it is located in a low-velocity zone, the diffused vapor tends

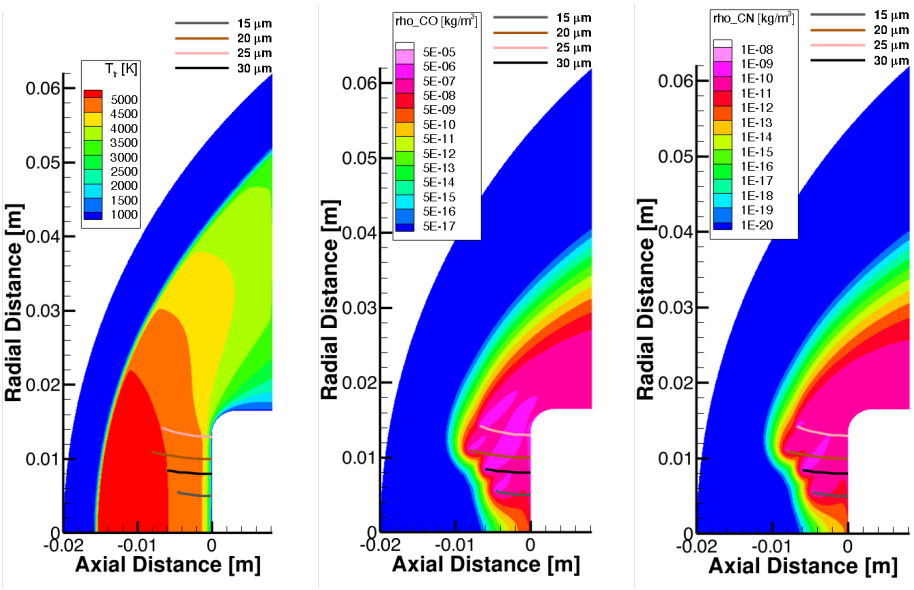

(a) Temperature (b) CO density (c) CN density

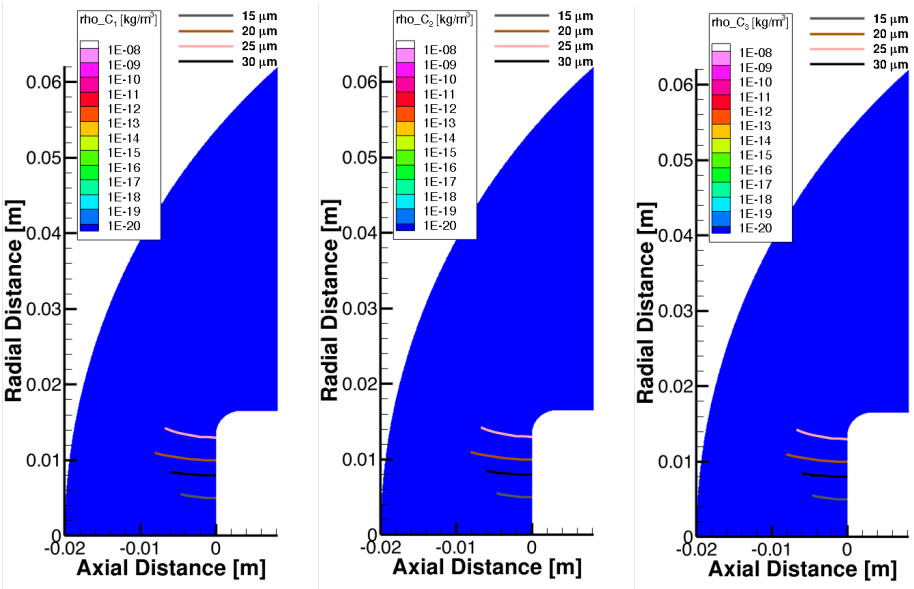

(d) C_1 density (e) C_2 density (f) C_3 density

Figure 27: Trajectories of the particles in a reacting air flow field at 0.09 ms with heterogeneous carbon reactions. (An animation of this figure is provided in the Supplementary Material.)

to move towards the centerline. The 20 µm and 25 µm particles also sublimate, contributing a very small amount of C_1, C_2, and C_3 vapors.

At 0.35 ms, 20 µm, 25 µm, and 30 µm particles are in the post-shock region, whereas the 15 µm particle

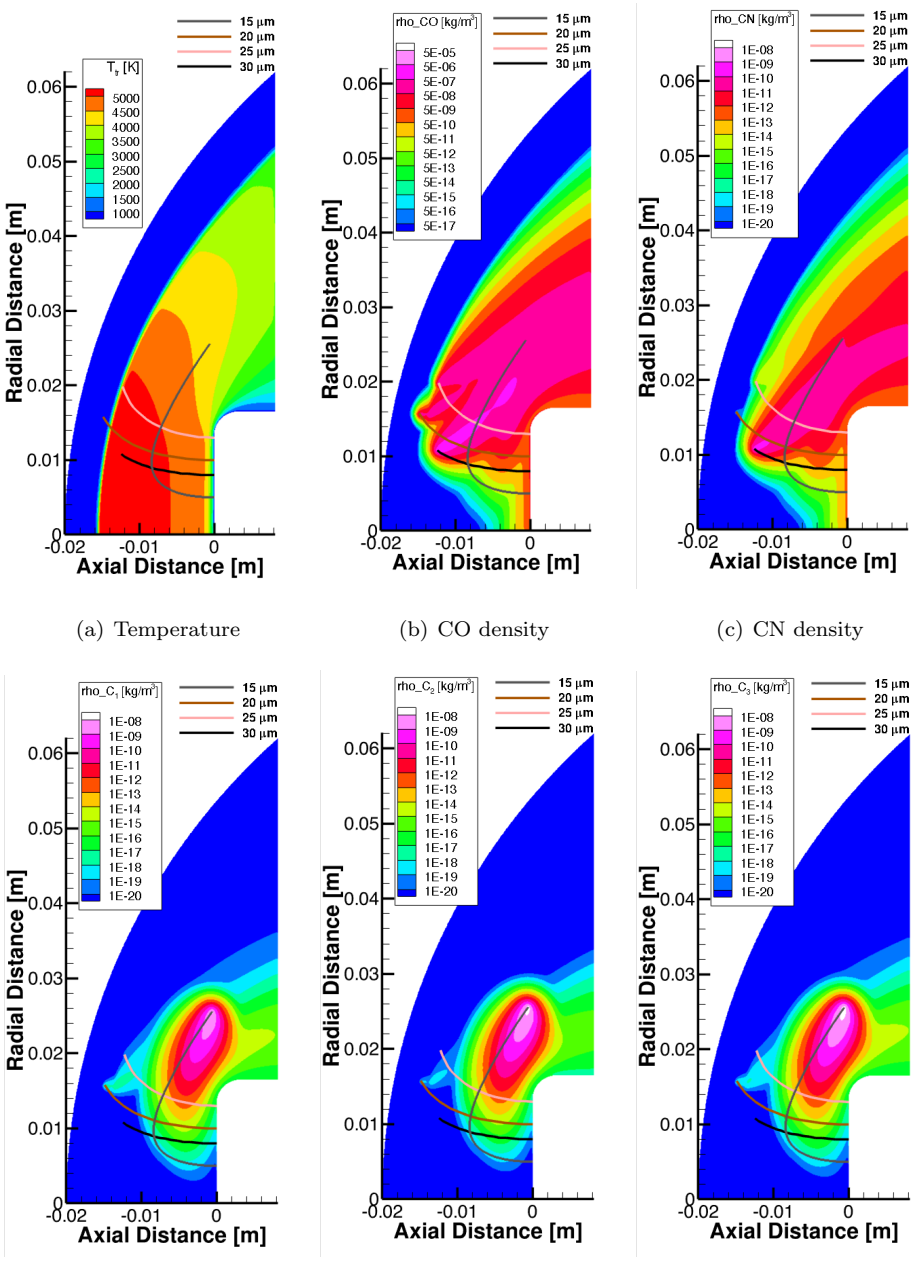

(a) Temperature (b) CO density (c) CN density

(d) C_1 density (e) C_2 density (f) C_3 density

Figure 28: Trajectories of the particles in a reacting air flow field at 0.19 ms with heterogeneous carbon reactions. (An animation of this figure is provided in the Supplementary Material.)

completes its travel, moving out of the computational domain. The CO vapor concentration decreases, and CN vapor becomes negligible. This behavior can be seen in Fig. 29. It is also observed that a small concentration of CO and CN remains close to the surface of the ablator.

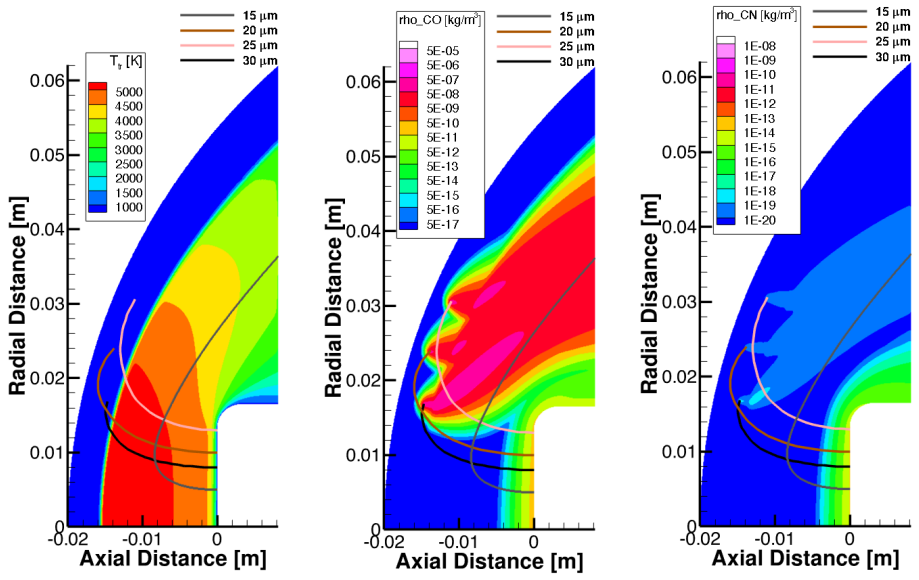

(a) Temperature (b) CO density (c) CN density

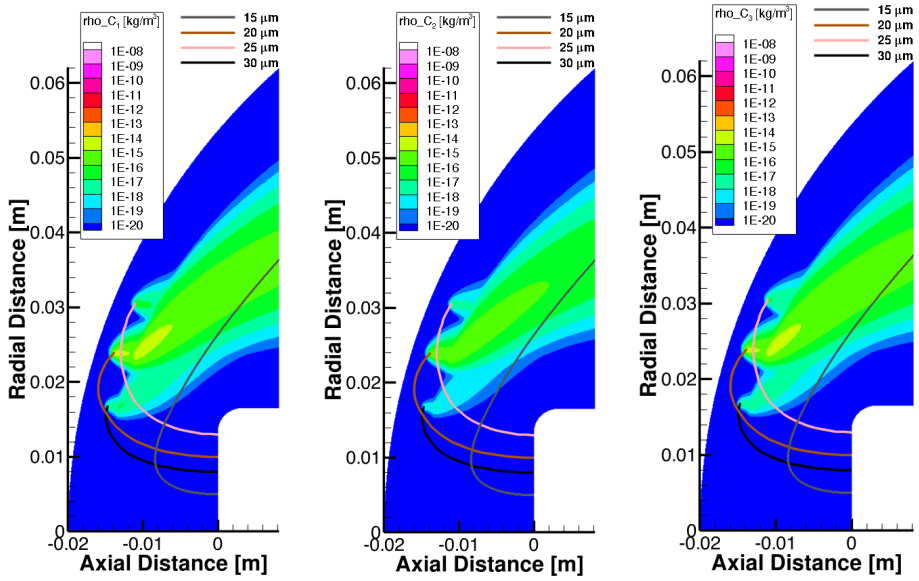

(d) C_1 density (e) C_2 density (f) C_3 density

Figure 29: Trajectories of the particles in a reacting air flow field at 0.35 ms with heterogeneous carbon reactions. (An animation of this figure is provided in the Supplementary Material.)

At 0.55 ms time, 20 µm particle exits the domain, and the other two particles (25 µm and 30 µm) enter the downstream region. The CO, CN, C_1, C_2, and C_3 concentrations seem to increase in magnitude, as illustrated in Fig. 30. However, a small amount of concentration of CO and CN remains close to the ablator.

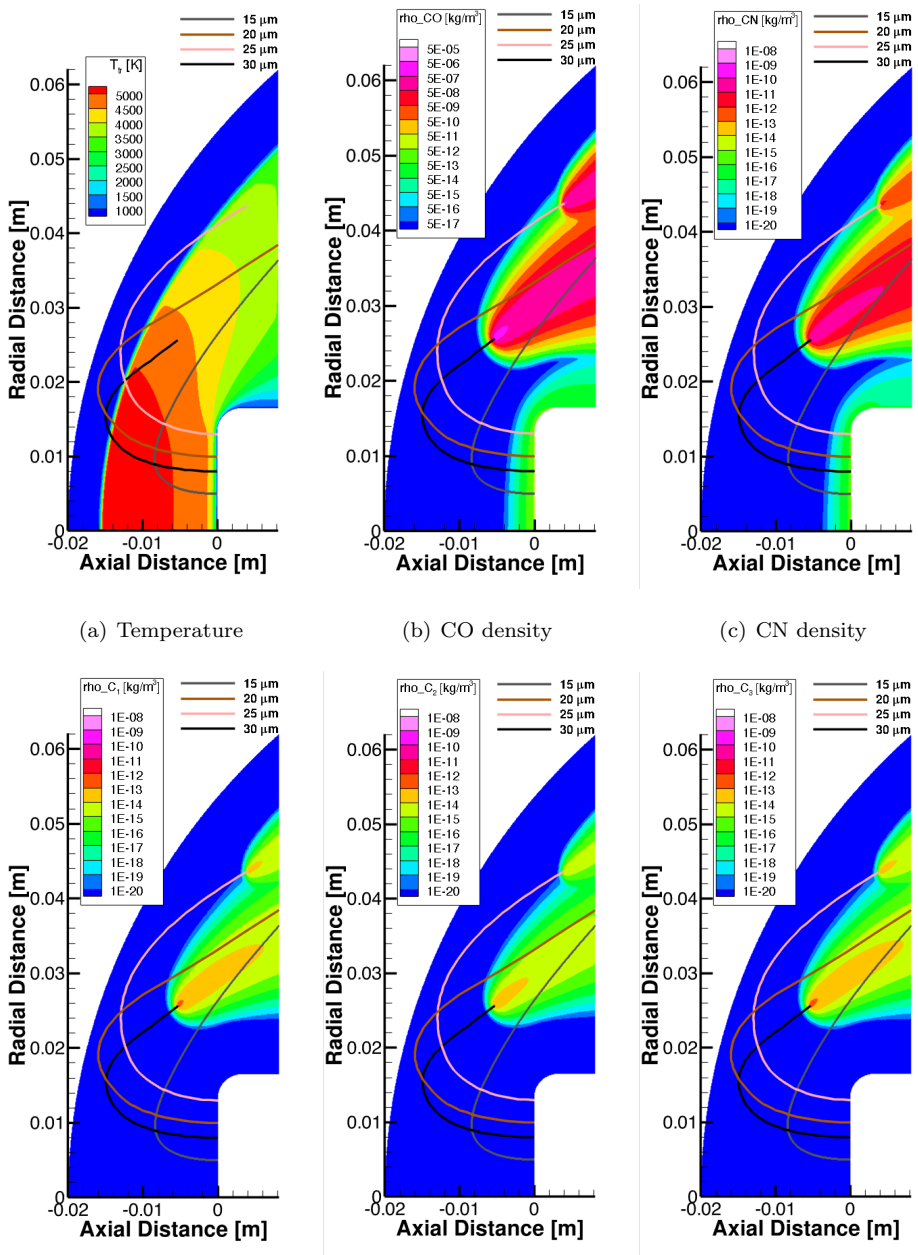

(a) Temperature (b) CO density (c) CN density

(d) C_1 density (e) C_2 density (f) C_3 density

Figure 30: Trajectories of the particles in a reacting air flow field at 0.55 ms with heterogeneous carbon reactions. (An animation of this figure is provided in the Supplementary Material.)

355 Apart from the effect on the composition of the flow field, the multiple particles simulation has a very small effect on the temperature and velocity fields. It is observed that the translational temperature changes by 0.3 K and vibrational temperature changes by 0.05 K. Also, the velocity field in the y-direction shows

regions of change in velocity in the post-shock region. Figure 31 illustrates these changes in the upstream region at 0.35 ms. The positions of the particles are shown in Fig.29 (a). It is noticed that there is a difference of 0.03 m/s of velocity in the y-direction.

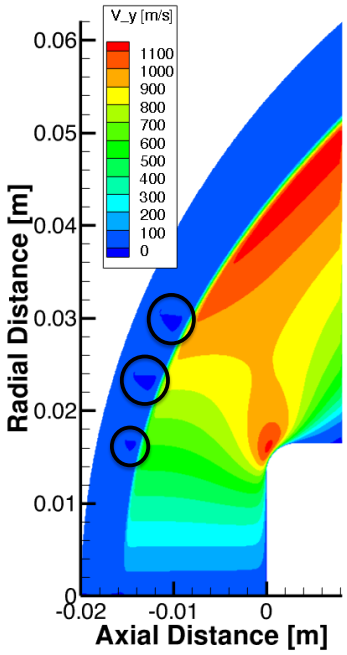

Figure 31: Flowfield Velocity in y-direction for the air simulation at 0.35 ms

The results from the multiple particle simulations illustrate that the products released from the particle convect and diffuse over a larger area. Although the number of particles in these simulations were three and four, the actual number in the spallation phenomena will be in the thousands. Therefore, the concentration of carbon products in total would be significant. The presence of this carbon vapor tends to increase the radiative heat flux directed toward the sample. Since these particles release vapor as they travel, the shift in the radiative heat flux is transient in nature. This also explains why the heat rates have been under-predicted in the downstream region in past studies. Therefore, evaluating the radiative heat flux contribution from these spalled particles is an essential exercise that will be performed in future work.

4. Conclusion

A two-way coupling was achieved using a Lagrangian particle trajectory code and a CFD code. The results obtained through this coupling allowed assessment of the spalled particle effect on the flow field.

Initially, the coupling was performed for a single particle spalled in Mach 5 argon and air environments. The results in the argon flow showed that the particle starts releasing the sublimate vapor once it crosses the shock, and its concentration keeps increasing as it moves through the computational domain. It was also observed that the magnitude of concentration of sublimate vapor increases from C_1 species to C_3 species at any point of the particle's travel. In an air environment, the particle reacts and releases the vapor soon after the ejection. It was observed that the particle releases CO vapor throughout its entire travel whereas CN vapor is released only in small quantities ahead of the shock. The sublimation of the particle follows the same trend as seen in the argon flow field. The magnitude of concentration of CO vapor released was higher than that of the other vapors. Additional gas-phase reactions were added to the CFD code and the same simulation was run. The results including added chemistry showed an increase in CN and C_1 vapor along with CO in the air environment. However, the coupling results show a very small change in temperature of about 0.01 K and no difference in the flow field velocity. To summarize the impact of the particle on the flow field, a parametric study was conducted. The study concluded that the closer the ejection position to the centerline and the lower the size and the ejection velocity, the more mass that is shed through chemical reactions. Similar behavior was also observed with the ejection angle of the particle decreasing from 90° to 0°.

The coupled simulation was also performed for multiple particles spalled in argon and air environments. The results for an argon environment showed a pattern similar to that of the single-particle simulation. The simulation for three particles showed that the vapor released was convected and diffused over a larger area and resulted in the change of temperature of 0.1 K. Similarly, for an air environment, the simulation was performed using four particles. The CO and CN vapor released diffused over a larger area, and a small concentration of these species remained close to the surface of the ablator. The particles also tend to sublimate in the post-shock region, and the concentration of the sublimate species increased as the particles moved through the computational domain. The particles that did not reach the shock sublimated near the surface.

These coupling results indicate a likely relationship between the presence of spalled particles and optical emissions, observed ahead of the shock. Also, the diffusive fluxes encompassed over larger areas provide a plausible explanation for the under-prediction of heat rates and temperature profiles in the downstream region.

5. Acknowledgements

Financial support for this work was provided by NASA Kentucky EPSCoR Award NNX10AV39A, and NASA award NNX13AN04A. The authors would like to thank L. P. Askins (University of Kentucky), P. Ghosh (VIT-AP), and D. A. Saunders (AMA, Inc.) for reviewing the manuscript.

References

[1] R. M. Wakefield, W. C. Pitts, Analysis of the heat-shield experiment on the pioneer-venus entry probes, in: 15th Thermophysics Conference, AIAA Paper 1980-1494, 1980. doi:10.2514/6.1980-1494.

[2] A. Balakrishnan, W. E. Nicolet, Galileo probe forebody thermal protection: Benchmark heating environment calculations, in: 16th Thermophysics Conference, AIAA Paper 1981-1072, 1981. doi:10.2514/6.1981-1072.

[3] F. S. Milos, Galileo probe heat shield ablation experiment, Journal of Spacecraft and Rockets 34 (1997) 705–713. doi:10.2514/2.3293.

[4] J. Moss, A. Simmonds, Galileo probe forebody flowfield predictions during jupiter entry, in: 3rd Joint Thermophysics, Fluids, Plasma and Heat Transfer Conference, AIAA Paper 1982-0874, 1982. doi:10.2514/6.1982-874.

[5] G. A. Raiche, D. M. Driver, Shock layer optical attenuation and emission spectroscopy measurements during arc jet testing with ablating models, in: 42nd AIAA Aerospace Sciences Meeting and Exhibit, AIAA Paper 2004-0825, Reno, Nevada, 2004. doi:10.2514/6.2004-825.

[6] T. Yoshinaka, Spallation Measurement at the Ablator Plasma Wind Tunnel Tests, Technical Report NASDA-TMR-970006E, National Space Development Agency of Japan, Tokyo, 1998.

[7] H. Kihara, M. Hatano, N. Nakiyama, K. ichi Abe, M. Nishida, Preliminary studies of spallation particles ejected from an ablator, Transactions of the Japan Society for Aeronautical and Space Sciences 49 (2006) 65–70. doi:10.2322/tjsass.49.65.

[8] C. B. Davies, C. Park, Trajectories of solid particles spalled from a carbonaceous heat shield, in: AIAA 20th Aerospace Sciences Meeting, AIAA Paper 1982-0200, Orlando, Florida, 1982. doi:10.2514/6.1982-200.

[9] C. Park, Interaction of spalled particles with shock layer flow, Journal of Thermophysics and Heat Transfer 13 (1999) 441–449. doi:10.2514/2.6482.

[10] S. Nozawa, H. Kihara, K. ichi Abe, Numerical investigation of spalled particle behavior ejected from an ablator surface, Transactions of the Japan Society for Aeronautical and Space Sciences, Aerospace Technology Japan 8 (2010) Pe_9–Pe_14. doi:10.2322/tastj.8.Pe_9.

[11] A. E. Pace, S. M. Ruffin, M. D. Barnhardt, A coupled approach for predicting radiation attenuation in particle-laced flows, in: 42nd AIAA Thermophysics Conference, AIAA Paper 2011-3771, Honolulu, Hawaii, 2011. doi:10.2514/6.2011-3771.

[12] M. J. Wright, G. V. Candler, D. Bose, Data-parallel line relaxation method for the navier-stokes equations, AIAA Journal 36 (1998) 1603–1609. doi:10.2514/2.586.

[13] R. S. C. Davuluri, H. Zhang, A. Martin, Numerical study of spallation phenomenon in an arc-jet environment, Journal of Thermophysics and Heat Transfer 30 (2016) 32–41. doi:10.2514/1.T4586.

[14] H. Zhang, H. Weng, A. Martin, Simulation of flow-tube oxidation on the carbon preform of pica, in: 52nd AIAA Aerospace Sciences Meeting, AIAA Paper 2014-1209, National Harbor, Maryland, 2014. doi:10.2514/6.2014-1209.

[15] A. Martin, S. C. C. Bailey, F. Panerai, R. S. C. Davuluri, H. Zhang, A. R. Vazsonyi, Z. S. Lippay, N. N. Mansour, J. A. Inman, B. F. Bathel, S. C. Splinter, P. M. Danehy, Numerical and experimental analysis of spallation phenomena, CEAS Space Journal 8 (2016) 229–236. doi:10.1007/s12567-016-0118-4.

[16] S. C. C. Bailey, D. Bauer, F. Panerai, S. C. Splinter, P. M. Danehy, J. M. Hardy, A. Martin, Experimental analysis of spallation particle trajectories in an arc-jet environment, Experimental Thermal and Fluid Science 93 (2018) 319–325. doi:10.1016/j.expthermflusci.2018.01.005.

[17] R. S. C. Davuluri, S. C. C. Bailey, K. A. Tagavi, A. Martin, Numerical reconstruction of spalled particle trajectories in an arc-jet environment, in: AIAA SciTech 2021 Forum, AIAA Paper 2021-1172, Virtual Event, 2021. doi:10.2514/6.2021-1172.

[18] H. Zhang, High Temperature Flow Solver for Aerothermodynamics Problems, Ph.d. thesis, University of Kentucky, Lexington, Kentucky, 2015. doi:10.13023/etd.2015.002.

[19] R. S. C. Davuluri, Modeling of spallation phenomenon in an arc-jet environment, Master's thesis, University of Kentucky, Lexington, Kentucky, 2015. doi:10.13023/etd.2015.001.

[20] M. Maclean, J. Marschall, D. M. Driver, Finite-rate surface chemistry model, ii: Coupling to viscous navier-stokes code, in: 42nd AIAA Thermophysics Conference, AIAA Paper 2011-3784, Honolulu, Hawaii, 2011. doi:10.2514/6.2011-3784.

[21] D. M. Driver, M. Maclean, Improved predictions of pica recession in arc jet shear tests, in: 49th AIAA Aerospace Sciences Meeting including the New Horizons Forum and Aerospace Exposition, AIAA Paper 2011-0141, Orlando, Florida, 2011. doi:10.2514/6.2011-141.

[22] R. L. Baker, Graphite sublimation chemistry nonequilibrium effects, AIAA Journal 15 (1977) 1391–1397. doi:10.2514/3.60806.

[23] A. Majid, Two Phase Flow Solver for Solid Particles in Hypersonic Martian Entry Flows, Ph.d. thesis, Universität Stuttgart, Stuttgart, Germany, 2011. doi:10.18419/opus-3855.

[24] A. Majid, U. Bauder, G. Herdrich, M. Fertig, Two-phase flow solver for hypersonic entry flows in a dusty martian atmosphere, Journal of Thermophysics and Heat Transfer 30 (2016) 418–428. doi:10.2514/1.T4542.

[25] C. Crowe, J. D. Schwarzkopf, M. Sommerfeld, Y. Tsuji, Multiphase Flows with Droplets and Particles, ISBN 978-0-42-910639-2, second ed., CRC Press, Boca Raton, Florida, 2011. doi:10.1201/b11103.

[26] A. Martin, E. D. Farbar, I. D. Boyd, Numerical modeling of the CN spectral emission of the stardust re-entry vehicle, in: 42nd AIAA Thermophysics Conference, AIAA Paper 2011-3125, Honolulu, Hawaii, 2011. doi:10.2514/6.2011-3125.

[27] A. Martin, I. D. Boyd, Modeling of heat transfer attenuation by ablative gases during the stardust reentry, Journal of Thermophysics and Heat Transfer 29 (2015) 450–466. doi:10.2514/1.T4202.

[28] G. P. Smith, D. M. Golden, M. Frenklach, N. W. Moriarty, B. Eiteneer, M. Goldenberg, C. T. Bowman, R. K. Hanson, S. Song, J. William C. Gardiner, V. V. Lissianski, Z. Qin, 1999, Gri-mech 3.0, URL: http://combustion.berkeley.edu/gri-mech/.